A search for the decays $B^+ \to \ell^+ \nu$ and $B^0 \to \ell^+ \tau^- \; (\ell = e, \mu)$ using hadronic tag reconstruction

Miika A. Klemetti

Master of Science

Department of Physics

McGill University

Montreal,Quebec

2007-24-11

A thesis submitted to the Faculty of Graduate Studies and Research in partial fulfillment of the requirements for the degree of Master of Science

Your file Votre référence
ISBN: 978-0-494-51293-7
Our file Notre référence
ISBN: 978-0-494-51293-7

DEDICATION

This document is dedicated to B. Yeung, as well as all financial institutions in Canada. Please bring the mortgage rates down!

ACKNOWLEDGEMENTS

I am grateful to the great luminosity and detector quality provided by the PEP-II and *BABAR* engineers and physicists that allowed the high-quality data acquisition. I thank my supervisor Steven H. Robertson, along with others, who provided valuable input throughout the analysis. Also, special thanks go to Philippe Roy and Tio Holtzman for their help and friendship, in and outside of the Physics Department.

ABSTRACT

We present searches for the leptonic decays $B^+ \to \ell^+\nu$ and the lepton flavor violating decays $B^0 \to \ell^\pm\tau^\mp$, where $\ell = e, \mu$, with data collected by the *BABAR* experiment at SLAC. These searches utilize a technique in which we fully reconstruct the accompanying $\overline{B}$ in $\Upsilon(4S) \to B\overline{B}$ events, and look for a monoenergetic lepton in the signal B frame. The signal yield in the data is extracted from a fit to the signal lepton candidate momentum distribution in the signal B rest frame. Using a data sample of approximately 378 million $B\overline{B}$ pairs ($342\,\mathrm{fb}^{-1}$), we find no evidence of signal in any of the decay modes. Branching fraction upper limits of $\mathcal{B}(B^+ \to e^+\nu) < 5.2 \times 10^{-6}$, $\mathcal{B}(B^+ \to \mu^+\nu) < 5.6 \times 10^{-6}$, $\mathcal{B}(B^0 \to e^+\tau^-) < 2.8 \times 10^{-5}$ and $\mathcal{B}(B^0 \to \mu^+\tau^-) < 2.2 \times 10^{-5}$, are obtained at the 90% confidence level.

ABRÉGÉ

Nous presentons une recherche de la desintegration leptonique $B^+ \to \ell^+\nu$ et de la desintegration ne conservant pas la saveur leptonique $B^0 \to \ell^\pm\tau^\mp$, ou $\ell = e, \mu$, avec les donnees recoltees par le detecteur *BABAR* au complexe SLAC. Ces recherches utilisent une technique par laquelle nous reconstruisons completement le hadron $\overline{B}$ accompagnateur dans des processus $\Upsilon(4S) \to B\overline{B}$, et nous cherchons un lepton monoenergetique dans la trame du B qui compose le signal. Le nombre d'evenement contribuant au signal dans l'echantillon de donnees est obtenu par un fit de la distribution de la quantite de mouvement du lepton candidat au signal, dans le referentiel inertiel du B provenant du signal. Utilisant un echantillon de donnees comprenant approximativement 378 millions de paires de $B\overline{B}$ ($342\,\mathrm{fb}^{-1}$), nous ne trouvons aucune evidence de signal dans aucun des modes de desintegrations observes. Des limites superieures aux taux de branchement suivants $\mathcal{B}(B^+ \to e^+\nu) < 5.2 \times 10^{-6}$, $\mathcal{B}(B^+ \to \mu^+\nu) < 5.6 \times 10^{-6}$, $\mathcal{B}(B^0 \to e^+\tau^-) < 2.8 \times 10^{-5}$ et $\mathcal{B}(B^0 \to \mu^+\tau^-) < 2.2 \times 10^{-5}$, sont obtenus avec un niveau de confiance de 90% .

TABLE OF CONTENTS

LIST OF TABLES

LIST OF FIGURES

CHAPTER 1
Introduction

The ultimate goal of particle physics is to create a theory capable of explaining the observable phenomena in our universe. While new models are constantly developed by ambitious theorists, only few of them pass the rigorous tests designed by the experimentalists. One of the great success stories in modern physics is the development of a model of electroweak and strong interactions, namely the Standard Model. Over the years the Standard Model has gained a general acceptance in the scientific community due to its great predictive power on particle interactions. This thesis drives forward the ongoing race to improve the precision of the known parameters in the Standard Model, while at the same time seeking evidence and constraints on new physics.

In this thesis, we describe searches for leptonic B meson decays $B^+ \to \ell^+\nu$ and $B^0 \to \ell^+\tau^-$ [1] using a data sample of 378 million $B\overline{B}$ pairs produced at the PEP-II B factory at Stanford Linear Accelerator Center in California, and recorded by the *BABAR* detector. These searches are characterized by the method of reconstructing the accompanying $\overline{B}$ in $\Upsilon(4S) \to B\overline{B}$ events, and looking for a monoenergetic lepton in the B frame.

Before explaining the analysis in greater detail, Chapter 2 goes over information about current physics models. Chapter 3 provides specific detail on the *BABAR* detector and the Monte Carlo simulations generated to study the *BABAR* detector's responses to background and signal events. Chapter 4 explains the principles of the reconstruction method, while rest of the signal selection criteria are detailed in Chapter 5. Chapter 6 discusses the various uncertainties involved in the analysis and their impact on the results obtained. The final results and their implications are discussed in Chapter 7.

CHAPTER 2
Theory

2.1 The Standard Model

Much of the current knowledge about particle interactions is accurately described by the Standard Model (SM). The SM describes three of the four fundamental forces of nature, including electromagnetism, the weak force and the strong force, but excluding gravity. The SM has been able to predict many physical observables with great precision, including the existence and properties of the Z and W bosons and the top, bottom and charm quarks.[1] These predictions are among many of the great successes of the SM, leading to its general acceptance among physicists. However, the SM has its shortcomings. The exclusion of gravity, the large number of free parameters, the unknown origin of the large mass differences between fermion generations, as well as the failure to explain the observed baryon asymmetry of the universe, are some of the most striking indications that the SM does not tell us the whole story. Indeed, it is generally agreed that the SM is only an effective theory of a more complete underlying theory. Before we dive into the New Physics (NP)

[1] These predictions were made by Kobayashi-Maskawa and Glashow-Weinberg-Salam models (GWS) of electroweak interaction. GWS, however, was eventually incorporated into the SM.

scenarios, that have the potential to offer better explanations to these questions, a quick review of the SM is in order.

As the SM is based on Quantum Field Theory (QFT), the particle interactions (i.e. dynamics) are described by a Lagrangian. Each particle is represented mathematically as a matter field, while the interactions between particles are represented by gauge fields that operate on the matter fields. The number of gauge fields is equal to the number of group generators and respects the gauge group symmetries associated with the given forces of nature. Thus, the SM Lagrangian can be split into components representing each force: $\mathcal{L}_{\mathrm{SM}} = \mathcal{L}_{\mathrm{QCD}} + \mathcal{L}_{\mathrm{Electroweak}}$, where QCD (Quantum Chomodynamics) describes the strong force and Electroweak describes the electromagnetism and weak force. The specific field content is described in more detail below.

2.1.1 Particle/Field Content

The matter fields (particles) in the SM are called fermions, each having a half-integer spin and thus obeying Fermi-Dirac statistics and the Pauli exclusion principle. Fermions can be grouped into leptons (l) and quarks (q), as is done in Table 2–1 (only quarks interact via strong force). Both leptons and quarks[2] can be organized into three generations, by grouping them in doublets according to the hypercharge $Y = 2(Q - T_z)$, where Q is the electric charge and T_z is the third component of the weak isospin. The significance of the generations will become evident in later

[2] All fermions, p, have anti-particles, $\bar{p}$, with the same mass and spin, but opposing quantum numbers.

sections. In the SM the neutrinos (ν) are considered to be massless. However, the recent observations of neutrino oscillations [2] (and, thus, of non-zero ν mass) require the SM to be modified slightly to include right-handed neutrinos. The implications of doing so will also be discussed in later sections.

The forces in the SM are mediated by gauge bosons, particles of integer spin. The EM force is carried by the massless photon (γ) and couples to all particles with an electric charge. The EM force has a local gauge symmetry of a $U(1)$ group. The weak force is mediated by $W^{\pm}$ and Z^0, and couples to all left-handed (right-handed) quarks and leptons (anti-quarks and anti-leptons). The weak interaction is the only interaction that provides flavor changing processes, and also the only interaction that violates parity. Together the EM and weak forces form the electroweak force with a symmetry $SU(2) \times U(1)$. At some high energy ($\mathcal{O}(300\,\mathrm{GeV})$), the $SU(2) \times U(1)$ is spontaneously broken down to $U(1)_{\mathrm{Q}}$ (Quantum Electrodynamics, QED), allowing the fermions and the $W^{\pm}$ and Z^0 gauge bosons to acquire masses. This symmetry breaking is facilitated by introducing a weak scalar doublet, a Higgs boson field (ϕ), with a potential $V(\phi) = \lambda(\phi^{\dagger}\phi - 1/2v^2)^2$, where v is the minima of the Higgs potential (i.e. the vacuum expectation value, vev). While this "Higgs mechanism" works to create the particle masses proportional to v, it does not explain the great variety of fermion masses (the values of each of the Yukawa couplings[3]) that we observe. As

[3] The coupling constant (h) of the interaction of type $V = h\bar{\psi}\phi\psi$ or $V = h\bar{\psi}\gamma^5\psi$, where ψ is a fermionic field.

a scalar boson, the SM Higgs does not carry any force and is not connected to any gauge symmetry.

The strong force is mediated by massless gluons and couples to particles with color charges of red, blue and/or green. The gauge symmetry of the strong force is SU(3). As each gluon carries a combination of color and anti-color charge, there are eight differently colored gluons.

All together, the SM is based on the gauge group $SU(3)_{\mathrm{c}} \times SU(2)_{\mathrm{L}} \times U(1)_{\mathrm{Y}}$, where the indices refer to color, left handed weak isospin and weak hypercharge respectively. The SM bosons are listed in Table 2–2. More detailed information (masses, quantum numbers, etc.) on these particles, fermions and boson, may be found in PDG 2006 [3].

Table 2–1: The SM matter particles, the fermions, divided into three generations.

	Generation 1	Generation 2	Generation 3
Quarks	Up (u) Down (d)	Charm (c) Strange (s)	Top (t) Bottom (b)
Leptons	Electron (e) Electron neutrino (ν_e)	Muon (μ) Muon neutrino (ν_μ)	Tau (τ) Tau neutrino (ν_τ)

2.1.2 Hadrons and Quark mixing

The interactions of quarks and gluons via the strong force are described by the QCD. All quarks carry a color charge and can be combined into color-neutral bound states called mesons and baryons. Mesons are $q\bar{q}'$ pairs of the same color and anti-color, while baryons are combinations of three quarks of different colors (red+blue+green=neutral). It is important to note that, the differing masses

Table 2–2: The gauge bosons in the SM mediate forces between particles, while the scalar Higgs boson is responsible for the generation of masses of the gauge bosons and fermions in the Standard Model [3].

	Gauge Bosons			Scalar Boson
Force	EM	Weak	Strong	-
Particle	Photon (γ)	Weak Gauge Bosons ($W^{\pm}, Z^0$)	Gluons (g_{ij})	Higgs (H^0)
Spin	1	1	1	0
Mass (GeV)	0	80.40 ± 0.03, 91.188 ± 0.002	0	> 114.4 (95% C.L.)

notwithstanding, the quark flavors have no play in the strengths of the QCD couplings (i.e. QCD is flavor blind). Mesons relevant to this paper are listed in Table 2–3, with the contributing quark flavors (i.e. u, d, c, s and b). No bound states (mesons or baryons) of the top quark have been observed.

Table 2–3: Common mesons with contributing quark flavors. The states with orbital excitations are usually expressed with a superscript '*' (i.e. K^*), with relevant exceptions for pions: ρ^+, ρ^0 and η^0; and heavy mesons like Υ(1S,2S,3S,4S).

Quarks	Meson	Masses
$d\bar{u}, d\bar{d} + u\bar{u}$	pions (π^-, π^0)	140 MeV, 135 MeV
$s\bar{d}, s\bar{u}$	kaons ($K^-, K^0_{\mathrm{S,L}}$)	494 MeV, 498 MeV
$c\bar{d}, c\bar{u}$	D-mesons (D^+, D^0)	1.869 GeV, 1.865 GeV
$b\bar{u}, b\bar{d}$	B-mesons (B^-, B^0)	5.279 GeV
$b\bar{b}$	$\Upsilon(4S)$	10.579 GeV

Since the neutral gauge bosons (γ, Z^0 and g_{ij}) conserve quark flavor, there exist no flavor changing neutral currents (FCNC) in the SM at the tree level. However, a flavor change either within a same generation of quarks, or between generations of quarks, can proceed through charged-current weak processes with $W^{\pm}$ (e.g. $uW^- \longrightarrow d$). The observed presence of quark-generation changing processes can be explained by introducing quark mixing, where quarks interact with the weak force according to weak eigenstates which differ from their mass eigenstates. In the SM, the origin of this mixing arises from the interaction of quarks with the scalar Higgs. The weak eigenstates are obtained by simultaneously diagonalizing the up and down-type quark mass matrices, leading to a set of weak couplings represented by the Cabibbo-Kobayashi-Maskawa matrix (V_{CKM}) [4]. By convention, probabilities for the down type quarks (d, s, b) are expressed in terms of their weak eigenstates (d', s', b') as defined below:

$$\begin{pmatrix} d' \\ s' \\ b' \end{pmatrix} = V_{\text{CKM}} \begin{pmatrix} d \\ s \\ b \end{pmatrix} = \begin{pmatrix} V_{ud} & V_{us} & V_{ub} \\ V_{cd} & V_{cs} & V_{cb} \\ V_{td} & V_{ts} & V_{tb} \end{pmatrix}, \begin{pmatrix} d \\ s \\ b \end{pmatrix}$$

where V_{CKM} can be parameterized with three mixing angles (the Euler angles, in the given representation) and a complex phase:

$$V_{\text{CKM}} = \begin{pmatrix} c_{12}c_{13} & s_{12}c_{13} & s_{13}e^{-i\delta} \\ -s_{12}c_{23} - c_{23}s_{23}s_{13}e^{i\delta} & c_{12}c_{23} - s_{12}s_{23}s_{13}e^{i\delta} & s_{23}c_{13} \\ s_{12}s_{23} - c_{12}c_{23}s_{13}e^{i\delta} & -c_{12}s_{23} - s12c_{23}s_{13}e^{i\delta} & c_{23}c_{13} \end{pmatrix},$$

where $s_{ij} = \sin\theta_{ij}$, $c_{ij} = \cos\theta_{ij}$, and $i\delta$ is the complex phase that introduces a violation in the charge-parity (CP) symmetry in weak processes. This is the only source of CP violation in the SM. Since the CKM matrix is unitary, we can construct a unitary triangle as is done in Figure 2–1. Figure 2–1 also shows the current experimental and theoretical limits on the various angles and the lengths of this triangle [5]. The element closely related to this paper is $V_{ub} = (4.31 \pm 0.30) \times 10^{-3}$ [3] (the smallest of the CKM matrix elements), which describes the transition from bottom quarks to up quarks.

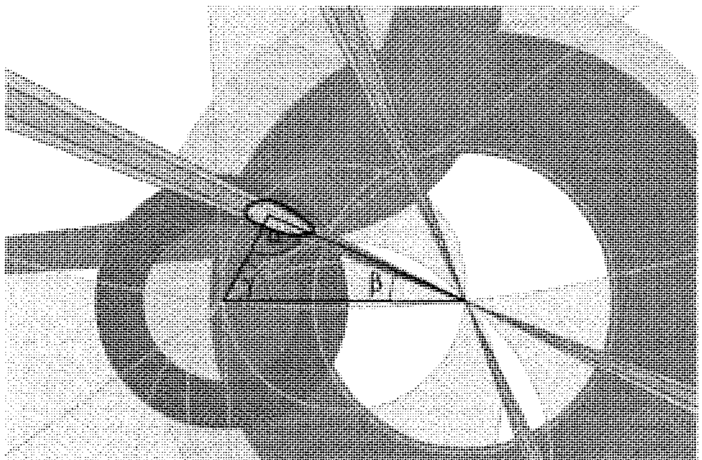

Figure 2–1: The CKM unitary triangle with its current experimental constraints. The constraints on the apex of the triangle (region surrounded by red line) is consistent with the SM predictions [5].

A matrix similar to the CKM matrix can be constructed for the leptonic sector as well. If we consider neutrinos to have masses, this matrix is non-diagonal, leading to mixing of leptons via weak interaction. Similar to the case with quarks, a superposition of the neutrino mass eigenstates associated with a charged lepton of given flavor would be considered a neutrino of that particular flavor. More detail on neutrino masses and their NP implications are provided in the next section.

2.2 New Physics

The SM is, at best, an incomplete description of particle interactions. While many alternate models (SUSY, leptoquarks, extra dimensions, 4^{th} generation of quarks, etc.) [6]. exist to explain some of the shortcomings of the SM, the experiments of today have only a limited sensitivity to observing direct evidence of the NP. Nevertheless, obtaining experimental bounds on rare decays has the potential to provide indirect constraints that may guide the development of the models. Below, we discuss two very popular extensions to the SM, both of which may be within the reach of experimental verification in the near future and which can be potentially significantly constrained from rare B decay measurements.

2.2.1 Two Higgs Doublet Models

In the SM there is nothing preventing the presence of more than one Higgs doublet. The extensions to the SM with two Higgs doublets are generally called Two Higgs Doublet Models (2HDM). The two Higgs doublets correspond to a total of eight degrees of freedom which, through symmetry breaking, lead to five physical Higgs particles. These particles are commonly named h^0, H^0, A^0 and $H^{\pm}$, where the first two neutral Higgs are CP-even ($M_{h^0} < M_{H^0}$) and A^0 is CP-odd.

The details of how the Higgs bosons couple with matter particles can vary significantly depending on the choice of model. One option is to have one Higgs doublet couple to both up and down type quarks, while another choice is to have each doublet to couple to either up or down type quarks separately. These scenarios are commonly named as 2HDM of type I and type II, respectively. In these scenarios additional constraints must be imposed to prevent FCNC from happening at tree level with rates inconsistent with the current experimental data. A third option is to allow both Higgs doublets to couple to both up and down-type quarks [7]. While it is possible to introduce additional global symmetries (such as R-parity in supersymmetric type-III 2HDM) to remove the FCNC at tree level, doing so may be unnecessary. It has been shown [8] that by very specific assumptions on the FC Yukawa couplings, the current experimental bounds on well measured quantities, such as $K^0 - \bar{K}^0$ mixing, could be satisfied.

2.2.2 Supersymmetry

An additional way to extend the SM is to allow an additional symmetry connecting the bosons and fermions. Unlike the SM, where fermions and bosons transform separately under tensor representations of the Poincare group (i.e. commutator and anticommutator relations), in supersymmetric (SUSY) models fermions and bosons are allowed to transform under spinor representations (supercommutators).

In such models each SM fermion has a bosonic "superpartner" and vice versa, effectively doubling the particle content of the model relative to the SM[4] . The neutral bosons in the SM, Z-boson, photon and neutral Higgs, have the fermionic superpartners zino, photino and Higgsino respectively. Since these SUSY particles have the same quantum numbers, they can mix with each other to form four "neutralino" mass eigenstates (χ^0). Similarly, the W-boson partner (wino) can mix with the

[4] The superpartners are named by prefixing a 's' in front of the SM particle name: squark ($\tilde{q}$), slepton ($\tilde{l}$), etc..

charged Higgsinos to form "charginos" ($\chi^{\pm}$). Neutralinos and charginos can couple with sparticles, the SM leptons and quarks, as well as with the Higgs-boson(s).

In the presence of the multitude of new particles, there exists many more channels for the SM particles to decay. While the SM decay rates may be either enhanced or suppressed as a result of the inclusion of SUSY contributions, many lepton flavor violating (LFV) and FCNC decays previously not permitted can also proceed via sfermion loops. Since SUSY sparticles are assumed to be heavy (allowing the SM-like physics to dominate at low energies), the Higgs should couple to sparticles more strongly than to the SM particles, allowing partial compensation for the possible loop suppressions.

Since there are no right-handed neutrinos at the electroweak scale, the earlier discussion about quark mixing cannot be directly generalized to the charged lepton sector. However, the presence of heavy right-handed neutrinos in the supersymmetric seesaw models allows off-diagonal elements in the slepton sector mass matrices, allowing for lepton flavor violation at rates much higher than provided by neutrino oscillations [9]. We will discuss this in more detail upon introduction of the $B^0 \to \ell^+ \tau^-$ decay mode.

In the simplest supersymmetric extension to the SM, the Minimal Supersymmetric Standard Model (MSSM), the Higgs sector consists of two scalar doublets (2DHM type II). In this model all Higgs couplings are proportional to the ratio of the vacuum expectation values of the two Higgs doublets, $\tan\beta = v_u/v_d$. This means that the mass of the Higgs can be constrained (or predicted) from the low-energy experimental data. Also, although the SUSY Lagrangian itself remains quite unknown at the electroweak scale, any experimental bounds on LFV or FCNC processes are especially useful for setting constraints on SUSY parameters. The specific differences in the SM and the MSSM predictions for leptonic B decays will be discussed in the next section.

Some of the advantages of SUSY models are the solution to the hierarchy problem (no fine-tuned corrections to particles' masses are needed), as well as the possible unification of the strong force to the electroweak interaction. It should be noted that while the SUSY soft breaking terms in the Lagrangian are actually independent of the SUSY particles, they could in principle arise from a more complete (but currently unknown) description of the SUSY symmetry breaking. Studying LFV and FCNC processes could thus shed light into the symmetry breaking mechanism itself. [10]

2.2.3 Baryon and Lepton numbers

While baryon (B) and lepton (L) numbers are conserved in the SM, it is not because of any fundamental physics principle. In SUSY models, however, B- and L-violating processes are present, unless additional global symmetries are imposed. One such symmetry is called the R-parity, $R_p = (-1)^{3B+L+2S}$, where S is the intrinsic spin of the particle. While R_p conservation is often required for the sake of consistency with the experimental non-observations of R_p violation, many models have considered direct R_p violation [11]. It has been shown that leptonic B^0 decays have a good potential to constrain the products of R_p- and lepton-flavor-violating coupling [12], yielding very strong bounds on each.

In Grand Unified (GU) theories there are additional symmetries that allow quarks and leptons to transform into each other. In such models, the rates of flavor changing processes such as $\tau \to e$ and $b \to d$ are related, and can be transformed into each other through GU symmetry transformations. This quality allows the measurements on leptonic FCNC processes to constrain FC processes involving the bottom quark [13].

The following section discusses the rare leptonic B decays in more detail, the SM predictions as well as the potential for NP contributions.

2.3 Leptonic B Decays

In this paper we present searches for the decays $B^+ \to \ell^+\nu$ and the lepton flavor violating decays $B^0 \to \ell^\pm\tau^\mp$, where $\ell = e, \mu$ decay modes are allowed in the Standard Model (SM) and the latter are not, both are potentially sensitive to NP effects, such as contributions by neutral and charged non-SM Higgs.

Searches for rare B decays with neutrinos in the final state are challenging due to the limited availability of kinematic constraints. However, purely leptonic B decays involving an electron or a muon possess a clear experimental signature in a form of a high momentum lepton. Combined with clean theoretical predictions due to the lack of QCD contributions in the final state, such leptonic B decays present an ideal place to test the SM against NP models.

2.3.1 Decay: $B^+ \to \ell^+\nu$

In the SM $B^+ \to \ell^+\nu_\ell$ decays involve an annihilation of $\bar{b}$ and u quarks into a virtual W^+ boson (Figure 2–2). According to the SM the branching fraction for this type of decay is given by:

$$\mathcal{B}_{\mathrm{SM}}(B^+ \to \ell^+\nu_\ell) = \frac{G_F^2 m_B m_\ell^2}{8\pi}\left(1 - \frac{m_\ell^2}{m_B^2}\right) f_B^2 |V_{ub}|^2 \tau_B, \tag{2.1}$$

where G_F is the Fermi coupling constant, m_ℓ is the lepton mass and m_B, τ_B and f_B are the mass, lifetime and decay constant for the B meson. $|V_{ub}|$ is the Cabibbo-Kobayashi-Maskawa (CKM) matrix element which describes the transition from b to u quarks. Within the SM, a determination of any one of the leptonic branching fractions represents a determination of the product $|V_{ub}| \cdot f_B$, which can be directly compared with determinations from lattice calculations, B-mixing and semileptonic decay measurements [14, 15, 16]. As seen in Equation 2.1, the decay rates are helicity suppressed by the factor ${m_\ell}^2$ resulting in SM predictions for the μ and e modes which are suppressed by factors of $\sim$ 250 and $\sim 10^7$ compared with the τ mode. Taking $\mathcal{B}(B^+ \to \tau^+\nu_\tau) = 1.31 \pm 0.48 \times 10^{-4}$ from the combination of recent *BABAR* and Belle results [17, 18] implies $\mathcal{B}_{\mathrm{SM}}(B^+ \to \mu^+\nu_\mu) \sim 5.2 \times 10^{-7}$ and $\mathcal{B}_{\mathrm{SM}}(B^+ \to e^+\nu_e) \sim 1.2 \times 10^{-11}$. NP contributions to these processes can enhance or suppress the decay rates compared to the SM, and may either preserve or violate the relative rates of the three leptonic modes depending on the particular NP model [19, 20].

The e and μ modes become particularly interesting in light of recent evidence for the $B^+ \to \tau^+\ \nu_\tau$ decay mode, for which the reported central value of $\mathcal{B}(B^+ \to \tau^+\nu)$ shows hints of disagreement with the SM prediction [21]. Currently, the most stringent published limits on $B^+ \to \ell^+\nu$ are from the Belle collaboration with $\mathcal{B}(B^+ \to e^+\nu) < 9.8 \times 10^{-7}$ and $\mathcal{B}(B^+ \to \mu^+\nu) < 1.7 \times 10^{-6}$ [22, 23, 24]. When comparing the predictions of the different decay modes, or even the predictions of different models, the large uncertainties in the f_B can be bypassed by calculating the ratio, as is done in:

$$R^B_{\rm SM} = \frac{\mathcal{B}_{\rm SM}(B^+ \to \ell^+\nu)}{\mathcal{B}_{\rm SM}(B^+ \to \tau^+\nu)}, \tag{2.2}$$

where the f_B dependence cancels out. Thus, the $\mathcal{B}$ predictions become precisely computable quantities which can be compared to experimental values.

In the MSSM models the H^+ contributions to $B^+ \to \ell^+\nu$ decays can be substantial, thanks to the helicity suppression in W^+ channels. Taking into account only tree level contributions, the ratio of the SUSY branching fraction to the SM branching fraction (Eq. 2.1) can be calculated to be

$$R_{B^+\to\ell^+\nu} = \frac{\mathcal{B}(B^+ \to \ell^+\nu)}{\mathcal{B}_{\rm SM}(B^+ \to \ell^+\nu_\ell)} = [1 - \frac{\tan^2\beta}{(1+\epsilon_0\tan\beta)}\frac{m_B^2}{m_H^2}]^2, \tag{2.3}$$

where $\tan\beta$ is the ratio of the vacuum expectation values of the two Higgs doublets ($\tan\beta = v_1/v_2$), and ϵ_0 is the effective coupling[5] ($\sim 10^{-2}$), and m_B is the mass of the B meson [21]. This correction is lepton flavor independent and, in type II modes, necessarily destructive.

Other NP effects, specifically LFV ones, can exist at one loop level, enhancing the individual decay rates and thus violating e–μ universality (possible loop diagrams are displayed in Figure 2–2). The LFV cases with the third generation neutrinos

[5] This is the effective coupling that parameterizes the non-holomorphic correction to the down-type Yukawa coupling, induced by a gluino exchange [25].

(e.g. $B^+ \to \mu^+ \nu_\tau$) are the most interesting since the larger τ Yukawa coupling will partially compensate for the loop suppression.

The above LFV loops are present in SUSY extensions and involve charged or neutral Higgs, neutralinos, charginos or sleptons. Assuming a charged Higgs exchange, the above ratio (Equation 2.2) can be re-calculated with a correction:

$$R^B_{\mathrm{LFV}} = R^B_{\mathrm{SM}} \left[1 + \left(\frac{m_B^4}{M_H^4} \right) \left(\frac{m_\tau^2}{m_{e,\mu}^2} \right) |\Delta_R^{31,32}|^2 \tan^6 \beta \right], \tag{2.4}$$

where $\Delta_R^{31,32}$ are the one-loop effective couplings that depend on ratios of SUSY masses [26]. Depending on the parameters used, the deviations in this ratio, from the SM values, are typically around $\sim 10\%$ for the muon mode. For the electron mode the LFV contributions can provide an order-of-magnitude enhancement. However, as the electron and muon modes have not yet been observed, we do not have an experimental value for R^B.

2.3.2 Decay: $B^0 \to \ell^+ \tau^-$

The LFV leptonic B decays, such as $B^0 \to \ell^+ \tau^-$ are forbidden in the SM in the absence of neutrino masses, but can occur via one-loop diagrams if neutrino oscillations are included (Figure 2–3). The rates of such processes, however, would be substantially below current or anticipated future experimental sensitivities. On the other hand, many extensions to SM such as SUSY Seesaw models provide great enhancements to the LFV decay rates [9]. The inclusion of SUSY transfers the LFV from the neutrino sector to the slepton sector, where the LFV is no longer suppressed by the scale of the low neutrino masses. In addition, in SUSY models $B^0 \to \ell^+ \tau^-$ becomes particularly interesting since Higgs-mediated decays involving third generation fermions are favored due to the larger Yukawa couplings. Such process allows the signal decay to proceed via a double penguin process (see Figure 2–3) [9], resulting in the branching fraction that can be approximated by:

$$\begin{aligned}\mathcal{B}(B^+ \to \ell_i \ell_j) &\sim \frac{G_F^4 M_W^4}{8\pi^5}|V_{tb}^* V_{td}|^2 M_B^4 f_B^2 \tau_B (\frac{m_b}{m_b + m_d})^2 \\ &\times \sqrt{(1 - \frac{(m_{\ell_i} + m_{\ell_j})^2}{M_B^2})(1 - \frac{(m_{\ell_i} - m_{\ell_j})^2}{M_B^2})} \\ &\times (1 - \frac{(m_{\ell_i} + m_{\ell_j})^2}{M_B^2})|c_S^{ij}|^2 + (1 - \frac{(m_{\ell_i} - m_{\ell_j})^2}{M_B^2})|c_P^{ij}|^2,\end{aligned}$$

where $V_{tb,td}$ are CKM elements for this FCNC decay. As for $B^+ \to \ell^+ \nu_\ell$, $V_{tb,td}$ are best obtained from $B\overline{B}$ mixing experiments [15], while f_B is obtained from lattice QCD calculations or B mixing experiments. The NP quantities are contained in the form factors, c_S^{ij} and c_P^{ij}, which are:

$$c_S^{ij} = c_P^{ij} = \frac{\sqrt{2}\pi^2}{G_F M_W^2} \frac{m_{l_j} \kappa_{bs}^d \kappa_{\ell_i \ell_j}^{*\ell}}{\cos^4 \beta \bar{\lambda}_{bs}^t} (\frac{sin^2(\alpha - \beta)}{M_{H^0}^2} + \frac{\cos^2(\alpha - \beta)}{M_{h^0}^2} + \frac{1}{M_{A^0}^2}), \tag{2.5}$$

where α is the mixing angle between the neutral h^0 and H^0 in SUSY Higgs sector. In our case, the index 'j' corresponds to τ. Thus, as seen by the m_j dependence, other lepton flavor violating decays are suppressed by the ratio m_j^2/m_τ^2. Between the decays $B^0 \to \mu^+ e^-$ and $B^0 \to \mu^+ \tau^-$ this ratio is approximately 0.0036. In the general flavor-universal MSSM, letting $\tan\beta = 60$ and assuming $\mathcal{B}(B_s \to \mu\mu) < 2 \times 10^{-6}$, the maximum branching fractions allowed for $B^0 \to \ell^+ \tau^-$ are at $\sim 2 \times 10^{-10}$ [9]. Such decays could be within the reach of a "Super B" factory with a data sample of 10 to 50 ab^{-1}. The current best experimental limits on the branching fractions for these two decays are $\mathcal{B}(B^0 \to e^+\tau^-) < 3.8 \times 10^{-5}$ and $\mathcal{B}(B^0 \to \mu^+\tau^-) < 1.1 \times 10^{-4}$, set by the CLEO collaboration with $10\,fb^{-1}$ of data [27].

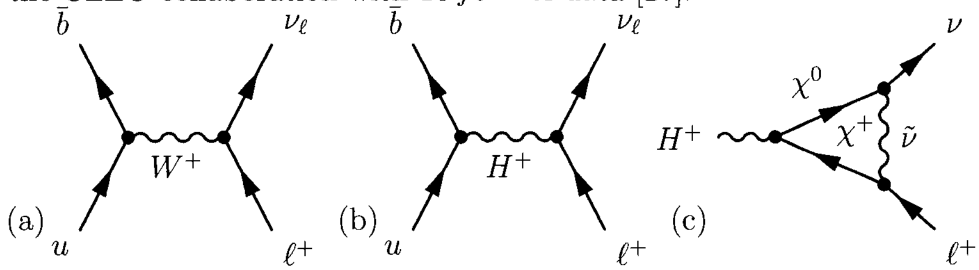

Figure 2–2: Feynman diagrams for the signal process (a) as predicted by the SM, and (b) possible contribution allowed by Supersymmetry. (c) represents one of the possible LFV (SUSY) process that could modify the relative rates between different leptonic modes.

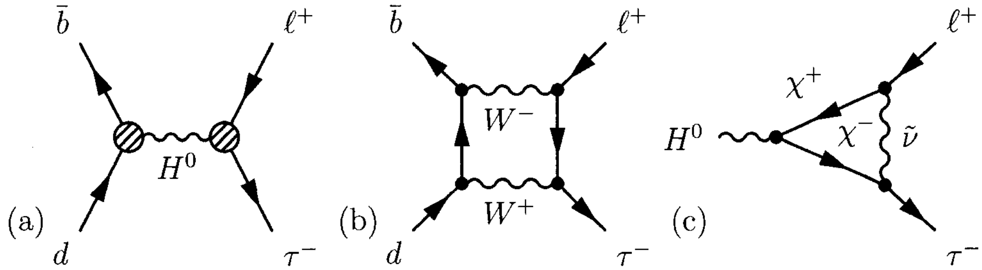

Figure 2–3: Feynman diagrams for the signal process via (a) Higgs mediated decay and (b) neutrino oscillation. (c) represents one of the lepton flavor violating processes present in the SUSY models [28].

CHAPTER 3
The *BABAR* detector and data simulation

3.1 SLAC and PEP-II

At the Stanford Linear Accelerator Center (SLAC), electron and positron beams are accelerated to energies of 9.0 GeV and 3.1 GeV respectively and injected into the PEP-II storage rings depicted in Figure 3–1. The counter rotating beams within the storage rings are then brought into collision by large magnets, creating physics events of great interest.

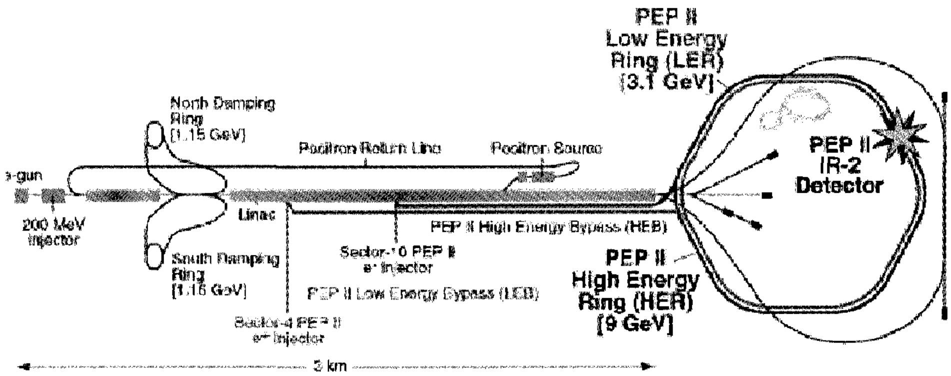

Figure 3–1: The SLAC beamline, followed by the PEP-II storage rings and the *BABAR* detector. First, the linear accelerator (linac) accelerates electrons and positrons to their desired energies. Then, the electron and positron beams are separated and directed, with magnetic fields, along the high- and low-energy rings respectively. The two beams are collided at the *BABAR* detector.

3.2 The *BABAR* detector

The *BABAR* detector is designed to detect particles resulting from e^- and e^+ collisions happening at the centre of mass (CM) energy of 10.58 GeV. This energy corresponds to the mass of the resonant state $\Upsilon(4S)$, which decays almost exclusively into B meson pairs. Since the e^+e^- collisions do not always result in a creation of a $\Upsilon(4S)$, there is a large amount of data for many specialized fields of study (such as τ physics.) However, the *BABAR* detector's design was largely dictated by the requirements of studying the various decay modes of the B mesons, and in particular to study time-dependent CP violation effects in such decays [29, 30].

For such studies it is important to have a detector capable of providing efficient and precise exclusive reconstruction of events. This requirement results in specific performance goals, including the following: the tracking must provide a vertex resolution of better than $< 80\ \mu m$, to offer $\overline{B}^0$-B^0 decay vertex separation; multiple scattering must be minimized in the inner detector and beam-pipe, by building the detector components with light materials, while withstanding a luminosity of $\mathcal{O}(3 \times 10^{33}\ cm^{-2}s^{-1})$; the kaon-pion separation must be better than $\sim 3\sigma$ over a momentum range consistent with $B \to DX$ $(D \to XY)$ and $B \to KX$ decays; and photons must be detected for a wide range of energies ($\sim 20\,\text{MeV} - 5\,\text{GeV}$). The various detector components are detailed below. The cross sections of the *BABAR* detector is shown in Figure 3–2.

3.2.1 Silicon Vertex Tracker

The Silicon Vertex Tracker (SVT) is designed for the detection and energy loss (dE/dx) measurement of charged particles. The particles traveling through any of

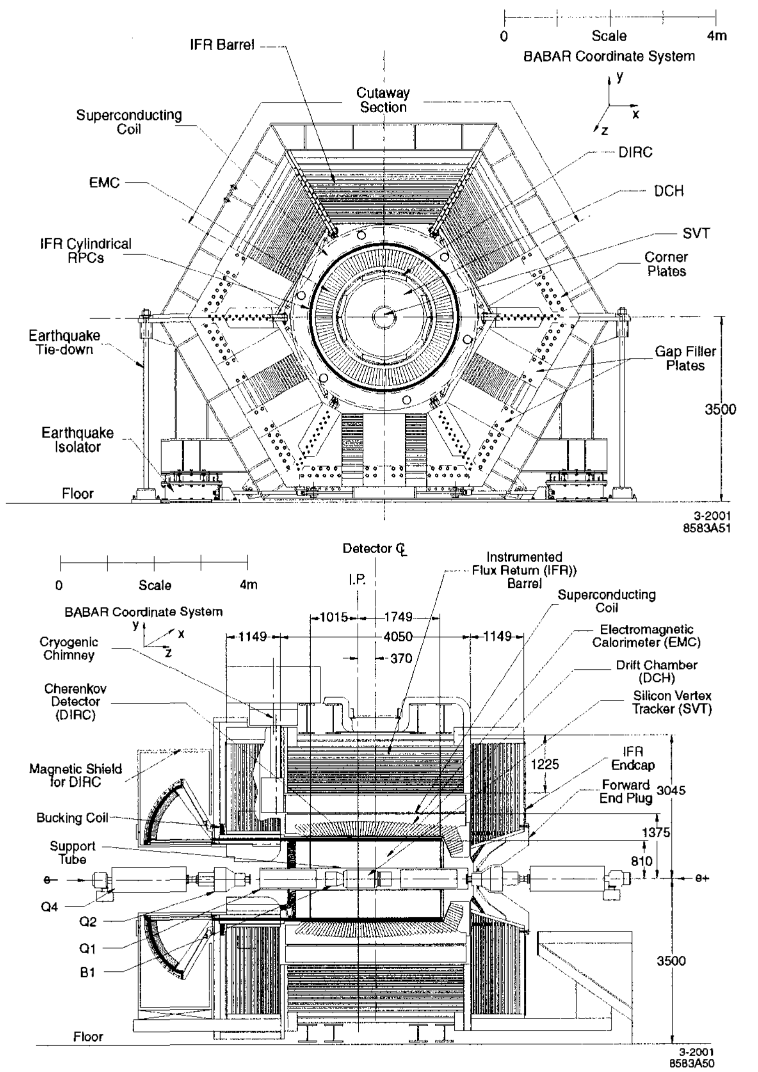

Figure 3–2: The *BABAR* detector's cross sections in the x-y plane (top) and the y-z plane (bottom).

the 1188 double-sided silicon strips deposit energy relative to their momentum and nature. By arranging the strips in five layers (each layer having slightly different silicon wafer design), a total of ten hits per track are accumulated allowing the trajectories of the particles to be determined with precision. All in all, there are ~140000 channels available, providing the resolutions of $< 130\ \mu m$ in Δz and $< 80\ \mu m$ in B vertexing. The inner three layers, where the closest one is located at a radius of 3.2 cm from the interaction point (IP), have a spatial resolution of $10 - 15\ \mu m$ allowing the angle and impact parameter measurements. The outer layers, up to 14.0 cm away from the IP, have a spatial resolution of about 40 μm and are used for tracking low transverse-momentum particles ($p_{\mathrm{T}} < 120\,\mathrm{MeV}$). The SVT provides an angular coverage of $17.1^{\circ} < \theta < 150^{\circ}$, as shown in Figure 3–3.

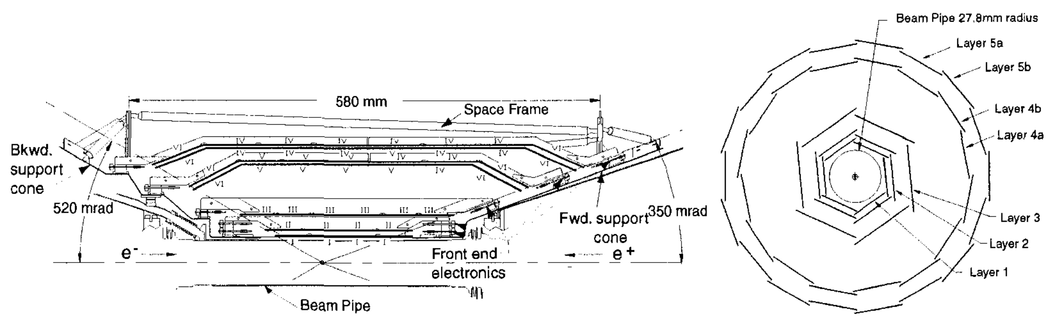

Figure 3–3: The *BABAR* SVT cross sections in the x-y plane (left) and y-z plane (right). The overlap of the layers (right) prevents particles escaping through gaps.

3.2.2 Drift Chamber

The drift chamber (DCH) is designed for charged particle tracking and identification. The *BABAR* DCH consists of a cylinder (length=280 cm, $\mathrm{rad}_{\mathrm{inner}} = 23.6\ cm$, $\mathrm{rad}_{\mathrm{outer}} = 81\ cm$) filled with helium and isobutane (80%, 20%). The traveling particles ionize the gas, and the resulting free electrons are collected by electric wires organized in 7104 hexagonal cells ($1.2 \times 1.8\ cm^2$), as depicted by Figures 3–4 and 3–5. The forward end-plate is about half the thickness of the rear end-plate ($24\ mm$) in order to minimize multiple scattering.

The 1.5 T field, created by superconducting solenoid, bends the tracks of charged particles allowing the particle momenta to be determined from the curvature of the track. The momentum resolution of the DCH ranges from $\sim 0.5\%$ for low p_{T} particles, to $\sim 1.5\%$ for high p_{T} particles[1] . The *BABAR* DCH provides a spatial resolution of $< 140\ \mu m$, as well as dE/dx resolution of 7%. Figure 3–6 shows the experimental dE/dx distributions for various particles with the theoretical predictions.

The information gathered from SVT and DCH is used together to reconstruct and identify the tracks in the event, and the results are passed on to the trigger system. The tracking efficiency is particle momentum dependent, varying from 93-98% for low momentum tracks to 98.8% for particles with a momenta of > 1 GeV/c.

3.2.3 Detector of Internally Reflected Cherenkov light

The Detector of Internally Reflected Cherenkov Light (DIRC) has the main function of distinguishing pions from kaons with momenta over 0.7 GeV/c, and protons with momenta of over 1.3 GeV/c. The DIRC works by detecting the Cherenkov light produced by charged particles traveling across a 4.9 m long ($1.7 \times 3.5\ cm^2$) quartz bar. The light is reflected internally, as shown in Figure 3–7 and projected at the surface of photomultiplier tubes. The 144 quartz bars are arranged in a 12-sided

[1] The uncertainty is calculated according to $\sigma_{p_{\mathrm{T}}}/p_{\mathrm{T}} = (0.13 - \frac{p_{\mathrm{T}}}{GeV/c} + 0.45)\%$

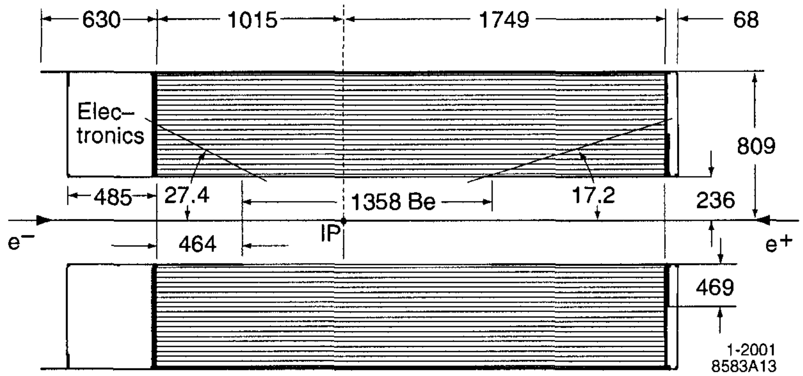

Figure 3–4: The *BABAR* DCH from the side. Six gold-plated aluminum "ground" wires (80 and 120 μm) surrounding the 20 μm gold-plated tungsten-rhenium wire (the "sense" wire). The sense wire is kept at 1960 V above the ground wires.

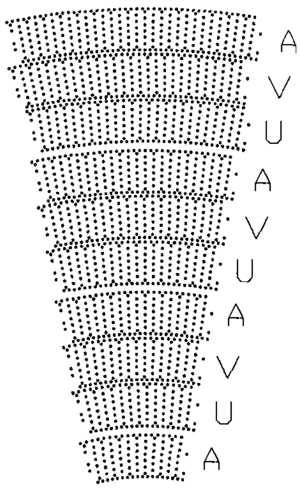

Figure 3–5: The cell layout of the *BABAR* DCH. The A, U and V represent the axial (A) and stereo (U,V) super-layers. The "stereo angle" ranges from 40 *mad* (innermost layer) to 70 *mrad* (outermost layer).

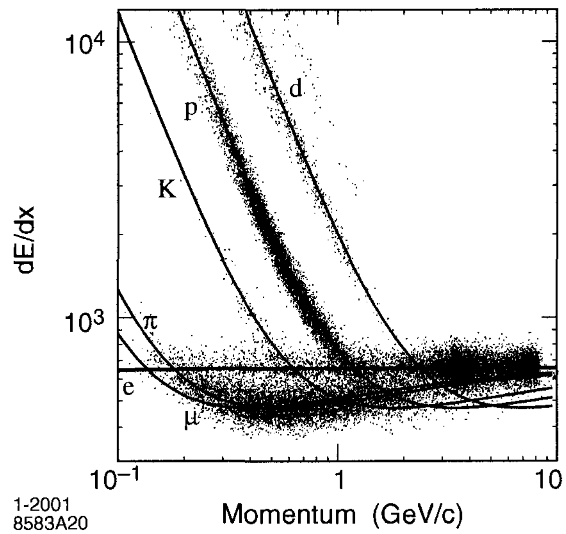

Figure 3–6: The experimental dE/dx distributions for various particles with the theoretical predictions (solid lines).

polygon surrounding the beam axis. The angle of the Cherenkov photons is dependent of the speed of the particle. The knowledge of the track angle and momentum (from DCH and SVT) can thus be used to determine the particle's mass.

3.2.4 Electromagnetic Calorimeter

The Electromagnetic Calorimeter (EMC) is designed to interact with photons and electrons, allowing the measurement of the energy and shape of the resulting particle showers (the shower energy is proportional to the energy of the incident electron/photon). If the resulting shower is associated with a track from the DCH, it is considered to be an electron, otherwise a photon. The *BABAR* barrel EMC is constructed of 5760 CsI(Ti) crystals, arranged in 280 modules of $300\mu m$ thick carbon-fiber composite material, providing an angular coverage of $15.8^o < \theta < 141.8^o$ (the forward end cap has another 820 crystals.) Figure 3–8 shows the layout and the

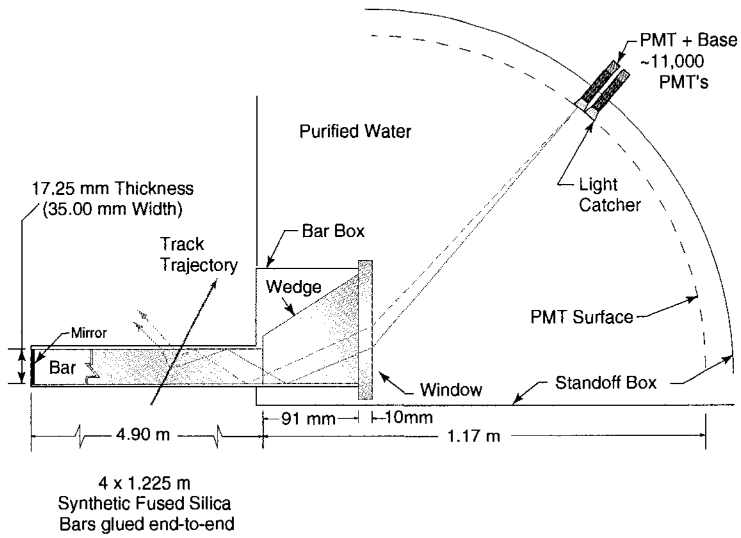

Figure 3–7: The *BABAR* DIRC.

cross section of the EMC crystals. The *BABAR* EMC is designed to be sensitive to electromagnetic showers from $\sim 20\,\mathrm{MeV}$ to over $10\,\mathrm{GeV}$, with an energy resolution of $\sim 7\%$ for low energy clusters, and $\sim 2\%$ for high energy clusters [2] .

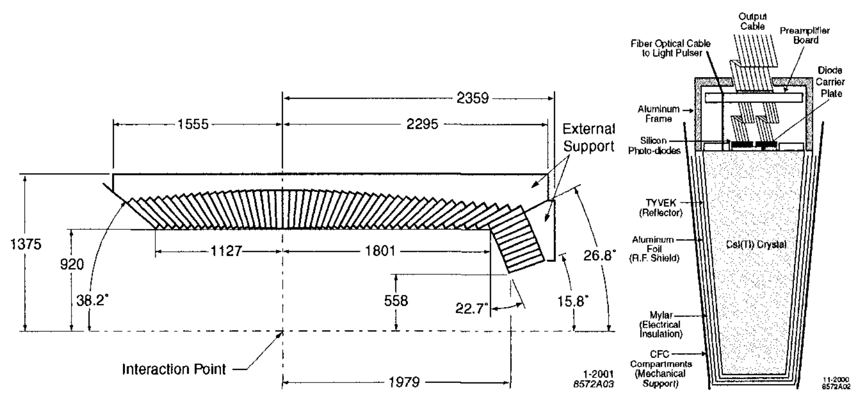

Figure 3–8: The *BABAR* EMC layout (left) and the cross section of the crystal (right).

[2] The uncertainty is calculated according to $\sigma_E/E = (1.25/\sqrt[4]{\frac{E}{GeV}} + 1.2)\%$

3.2.5 Instrumented Flux Return

Instrumented Flux Return (IFR) is designed to detect muons and neutral hadrons. It consists of a barrel and two end caps, with Resistive Plate Chambers (RPC) located in the gaps of 18 solenoid magnetic flux return material. A gas mixture within the RPC (isobutane, argon and freon) is ionized by muons passing through. The resulting free ions are then collected by graphite sheets, of potential difference 8 kV, enclosing the gas chambers. If such RPC cluster is consistent with hits in adjacent IFR layers and can be associated with a track from the DCH and SVT, a muon identification is passed. Otherwise the particle is assumed to be a neutral hadron interacting with the flux return material, and producing showers of charged particles detectable by the RPCs.

An upgrade to the muon and neutral hadron identification was implemented during the summer 2006, by replacing some of the RPC with Limited Streamer Tubes (LST). LSTs consist of silver plated wires placed in the centers of $9 \times 9\ cm^2$ tubes. Units of eight such cells are arranged together and coated with a protective layer of graphite. These units are then placed in plastic tubes holding a non-explosive CO_2 based gas. Heavy particles traveling through the LST create a charge in the gas which is collected by the wires at $\sim 4.7kV$, generating a signal pulse. Each of the units has their own high voltage feed, originating from the outside of the detector. The front end electronics are also kept at the outside of the detector to allow easier maintenance and repairs. The benefits of the LST design are the high efficiency and reliability (proven by ZEUS, LEP experiments, and CLEO among many others) over many years of operation. Also, high modularity and possibility to replace dead units is important, as opening the *BABAR* detector is a task requiring large amount of detector down time.

3.2.6 Trigger System

The function of the trigger system is to determine which events, as observed by the *BABAR* detector, are recorded for future use. The *BABAR* trigger does this in two stages, filtering out events judged to be of lesser interest to the analysts. The first trigger level (L1) requires the presence of tracks or clusters in the event, as measured by the DCH and the EMC. The information from the DCH (tracks) and EMC (calorimeter towers) is processed together to arrive at a L1 trigger decision. The L1 trigger rate is typically $2.5\ kHz$ at the luminosity of $8 \times 10^{33}\ cm^{-2}s^{-1}$[3].

The next trigger level (L3) uses the combined information from all of the detector subsystems to refine the sample. The L3 trigger also selects events used for calibration purposes, online monitoring tasks, as well as performs vetoes on Bhabba and 2γ events. The events passing the trigger system are recorded by 28 dual Pentium-III 1.4 GHz computers, at the rate of $\sim 200\ Hz$ corresponding to approximately at $4\ ms$ per event.

3.3 Data and Monte Carlo Simulation

The searches described in this work are based on a data sample of approximately 378 million $B\overline{B}$ pairs, corresponding to an integrated luminosity of $342\,\mathrm{fb}^{-1}$ collected

[3] A level-2 (L2) trigger was foreseen in the original design, but improvements in computing technology made it unnecessary by the time the trigger system was actually built

at the $\Upsilon(4S)$ resonance by the *BABAR* detector. Monte Carlo (MC) simulated data samples are created in order to study the detector responses in better statistical detail. The MC simulation of the *BABAR* detector is based on GEANT4 [31].

MC samples are produced for both signal and background events, allowing the estimation of the signal selection efficiencies and the background rates. The sample sizes, cross sections and corresponding luminosities for each MC sample are shown in Table 3–1. Table 3–2 shows the integrated luminosities of the data and MC samples. The onpeak data is accumulated at the $\Upsilon(4S)$ resonance and the offpeak at about $\sim 40\,\mathrm{MeV}$ below the centre-of-mass energy of this resonance.

Table 3–1: MC samples for signal and background events, with sample sizes and corresponding luminosities where applicable. The branching fractions for the signal modes are set at 10^{-5}.

Signal MC Samples	σ/nb	L/fb^{-1}	Events ($\times 10^5$)
$B^+ \to \mu^+\nu_\mu$ vs generic B^-	$\sim 1.05 \times 10^{-5}$	1.04×10^5	10.90$\times$
$B^+ \to e^+\nu_e$ vs generic B^-	$\sim 1.05 \times 10^{-5}$	1.04×10^5	10.90$\times$
$B^0 \to \mu^+\tau^-$ vs generic B^0	$\sim 1.05 \times 10^{-5}$	1.04×10^5	6.28
$B^0 \to e^+\tau^-$ vs generic B^0	$\sim 1.05 \times 10^{-5}$	1.04×10^5	6.28
Background Samples	σ/nb	L/fb^{-1}	Events ($\times 10^8$)
Generic B^+B^-	0.525	1060.561	5.57
Generic $B^0\overline{B}^0$	0.525	1059.718	5.56
Generic $c\bar{c}$	1.3	468.604	6.09
Generic uds	2.09	338.583	7.08
Generic $\tau^+\tau^-$	0.94	317.755	2.99

Table 3–2: Sample sizes (in fb^{-1}) broken down by run. For the analysis, each of the samples are normalized to the luminosity of the onpeak sample of the corresponding run.

	Data		MC				
Run #	Offpeak	Onpeak	B^+B^-	$B^0\overline{B}^0$	uds	$\tau^+\tau^-$	$c\bar{c}$
1	2.4	19.9	132.6	131.9	41.8	39.1	63.3
2	6.8	59.6	196.1	196.4	60.4	59.5	125.5
3	2.4	32.3	89.7	96.3	32.0	29.8	60.2
4	10.0	97.9	320.6	318.2	102.0	94.9	120.8
5	14.6	133.0	32.2	316.9	102.3	94.5	98.8
Total	36.1	342.6	1060.6	1059.7	338.6	317.8	468.6

CHAPTER 4
Exclusive Tag B Reconstruction

The data and MC events are analyzed using a specialized package (`BRecoilUser` of `Analysis-32`, release 18.6.xx) available for *BABAR* analysts. The `BRecoilUser` is a package configured for analyses with a reconstructed $B^{\pm}$ or B^0, and retrieves required event information for a sub-sample of all detector data that satisfy certain physics requirements (`BSemiExcl` Skim). In `R18b` `BSemiExcl` skimmed events, the B meson is reconstructed exclusively with a minimum requirement of three charged tracks in the detector. This approach has previously been applied on other decay modes [32, 33, 34]. Because the two B mesons are produced with very little momentum in the CM frame, $B\overline{B}$ events typically produce a more isotropic distribution of particles in the detector than non-resonant ("continuum") backgrounds. Such backgrounds ($e^+e^- \rightarrow f\bar{f}$, where f represents u,d,s or c or any charged lepton) are suppressed by requiring R2<0.5, where R2 is the ratio of the second to the zeroth Fox-Wolfram moment [35], computed using all charged and neutral particles in the event. The charged tracks are obtained by the SVT and DCH and are assigned particle hypotheses based on information from other detector subsystems. K^0_S candidates are selected by combining oppositely charged $\pi^{\pm}$ candidates and requiring that the π^+ π^- invariant mass satisfies $0.47\,\mathrm{GeV}/c^2 < m_{\pi^+\pi^-} < 0.52\,\mathrm{GeV}/c^2$. π^0 candidates are obtained from the combination of EMC clusters with no associated tracks, each with $\Upsilon(4S)$ CM-frame energies greater than 50 MeV, for which the $\gamma\gamma$ invariant mass satisfies $115\,\mathrm{MeV}/c^2 < m_{\gamma\gamma} < 150\,\mathrm{MeV}/c^2$. Over 96% of the time the $\Upsilon(4S)$ resonance decays into a pair of B mesons. A collection of the tracks and clusters, recorded by the detector, are combined in order to fully reconstruct one of the B mesons (only fully hadronic modes involving $\overline{D}$ or $\overline{D}^*$ are considered). The combination of particles with an energy closest to the nominal B energy, resulting from the given beam energy, is chosen as the tag B candidate, B_{tag}. The other B is labeled as the signal B, B_{signal}.

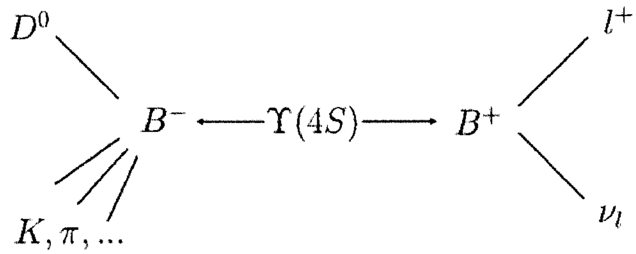

Figure 4–1: $\Upsilon(4S) \to B^+B^-$ is reconstructed exclusively. By combining the momentum 4-vectors of D^0 with charged and neutral hadrons (pions and kaons), the momentum vector of B_{tag} can be determined. By energy-momentum conservation, the momentum of the accompanying B_{signal} is completely determined.

As B mesons decay mostly by hadronic modes involving a D^-, D^0, $D^{*\pm}$, or a D^{*0} ($B^\pm \to D^{(*)0}X$, $B^0 \to D^{(*)\pm}X$), the number of decay modes is very large. As an example, the modes involving only pions are listed in Table 4–1. The presence of kaons makes the situation even more complicated. In general, the reconstruction starts with a $D^{(*)0}$ or $D^{(*)\pm}$ seed. $D^{(*)0}$ is reconstructed from decays $D^0 \to K^-\,\pi^+$, $D^0 \to K^-\,\pi^+\,\pi^0$, $D^0 \to K^-\,\pi^+\,\pi^+\,\pi^-$ or $D^0 \to K^0_S\,\pi^+\,\pi^-$; and $D^{*0} \to D^0\,(\pi^0, \gamma)$. Similarly, the $D^{(*)+}$ is reconstructed in the modes $D^+ \to K^-\,\pi^+\,\pi^+$, $D^+ \to K^0_S\,\pi^+$, $D^+ \to K^0_S\,\pi^+\,\pi^0$, $D^+ \to K^-\,\pi^+\,\pi^+\,\pi^0$ or $D^+\,K^0_S\,\pi^+\,\pi^+\,\pi^-$; and $D^{*+} \to D^+\,\pi^0$.

The X is formed by combining some of the left over pions and kaons. The combination of the X and D with a lowest value of $\Delta E = |E_B - E_{\text{beam}}|$, that satisfies the condition $-0.2 < \Delta E < 0.2\,\text{GeV}$, is chosen as the B_{tag} candidate (E_B is the energy of the reconstructed B and $E_{\text{beam}} = E_{\text{CM total}}/2$ is the beam energy, both in the CM frame.) All in all, the exclusive reconstruction algorithm finds up to six daughters for the B_{tag} in addition to the $D^{(*)}$ candidate [36].

Table 4–1: The $B^0 \to D^{*+}X^-$ decay modes involving only pions.

Decay
$B^0 \to D^{*+}\pi^-$
$B^0 \to D^{*+}\rho^-$
$B^0 \to D^{*+}\pi^-\pi^0$
$B^0 \to D^{*+}a^-{}_1$
$B^0 \to D^{*+}\pi^-\pi^-\pi^+$
$B^0 \to D^{*+}\pi^-\pi^0\pi^0$
$B^0 \to D^{*+}\pi^-\omega$
$B^0 \to D^{*+}\pi^-\pi^-\pi^+\pi^0$
$B^0 \to D^{*+}\pi^-\pi^0\pi^0\pi^0$
$B^0 \to D^{*+}\pi^-\pi^-\pi^+\pi^+$
$B^0 \to D^{*+}\pi^-\pi^-\pi^+\pi^0\pi^0$
$B^0 \to D^{*+}\pi^-\pi^-\pi^+\pi^-\pi^+\pi^0$
$B^0 \to D^{*+}\pi^-\pi^-\pi^+\pi^0\pi^0\pi^0$

Previous B factory searches for $B^+ \to \ell^+\nu$ and $B^0 \to \ell^+\ \tau^-$ have used an inclusive method in which the accompanying B is not explicitly reconstructed [22, 23, 24]. Instead, the events are searched for a high momentum lepton candidate. If one is found, the rest of the particles are assumed to be originating from the "other" B meson. While such method results in a significantly higher signal selection efficiency, it suffers from a substantially increased background compared with the exclusive reconstruction method presented here.

The efficiency of reconstruction for signal events is approximately $\sim 0.25\%$ for charged B mesons and $\sim 0.20\%$ for neutral B mesons. With the current level of luminosity, the inclusive method provides better limit sensitivity. However, due to the very low background achievable with the exclusive method, the branching fraction at which the two methods would have the potential to report a signal observation are comparable. If a higher luminosity $e^+e^- \to \Upsilon(4S)$ facility becomes available in the future, the method described in this thesis may prove to be the preferred approach for the high-precision studies of leptonic B decays.

4.0.1 Additional Requirements on B_{tag}

Naturally, we require the B_{tag} candidate, given by the semiexclusive reconstruction, to have a charge which is consistent with the expected signal decay (i.e. neutral for the $B^0 \to \ell^+\tau^-$ search and $\pm$ for the $B^+ \to \ell^+\nu$ search). The mass of the B_{tag} is calculated according to energy substitution

$$m_{\text{ES}} = \sqrt{E_{\text{beam}}^2 - \vec{p}_B^{\,2}}, \tag{4.1}$$

where E_{beam} is the beam energy and $\vec{p}_B$ is the momentum the B_{tag} candidate in the CM frame. For a correctly reconstructed B_{tag}, this quantity must be close to the nominal B meson mass of $5.279\,\text{GeV}/c^2$. Additionally, we record a sample of events in the m_{ES} sideband region ($5.220 < m_{\text{ES}} < 5.265\,\text{GeV}/c^2$), to allow for studies of combinatorial background events. The signal and background distributions for this variable are shown in Figure 4–2. If the reconstruction process were perfect, the m_{ES} distribution would be a delta function at the B meson mass $m_B \sim 5.279\,\text{GeV}/c^2$. The resolution in m_{ES} is dominated by the spread in E_{beam}, $\sigma_{E_{\text{beam}}} \approx 2.59 MeV$. The large combinatorial tail showing in Figure 4–2 disappears once the signal-side requirements are applied. Figure 4–3 demonstrates this by showing the m_{ES} distribution after the requirements on the signal lepton momentum. The distributions for the quantity

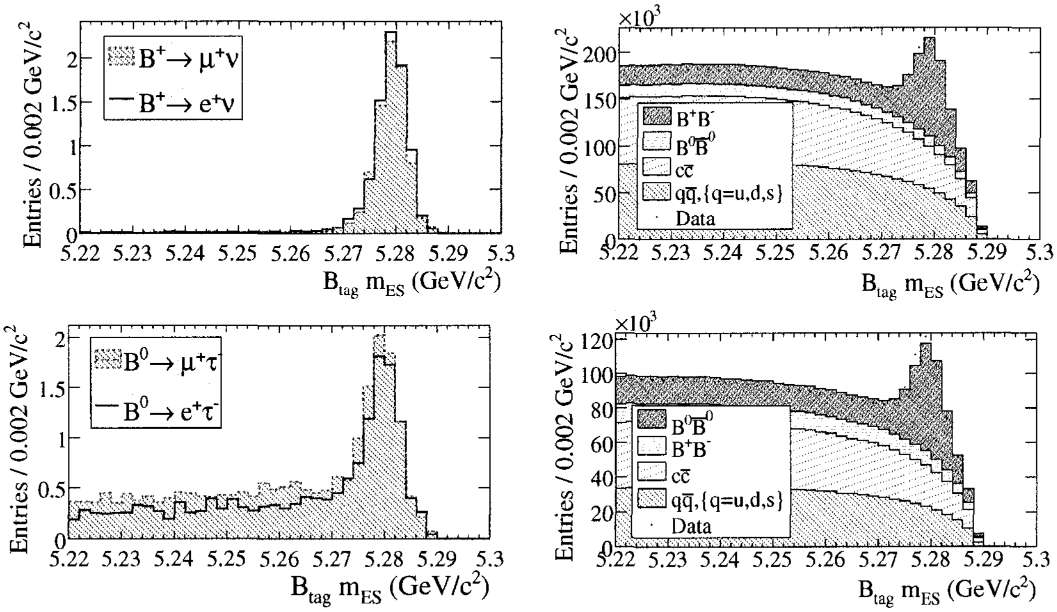

Figure 4–2: m_{ES} distributions of B_{tag} candidates for B^+B^- (top) and $B^0\overline{B}^0$ (bottom). The signal MC are shown on the left and the background MC with the data on the right. The events are required to have one reconstructed B of correct charge. In these plots the signal mode branching fractions are set to 10^{-5}.

$|\cos\theta_{\mathrm{T}}|$, which represents the inner product of the thrust vectors of the reconstructed B and the rest of the particles recorded by the detector, are shown in Figure 4–4. Thus, the distribution of $|\cos\theta_{\mathrm{T}}|$ is determined by the event topology of the $\Upsilon(4S)$ decay. For $B\overline{B}$ events the distribution is rather flat (spherical symmetry), while for decays to lighter particles such as $q\overline{q}$ pairs $|\cos\theta_{\mathrm{T}}|$ peaks for values close to one (representing back-to-back jets). A requirement of $|\cos\theta_{\mathrm{T}}| < 0.90$ is used to

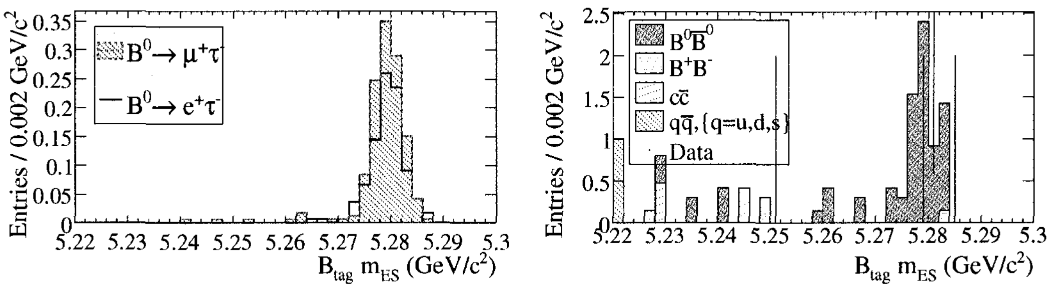

Figure 4–3: m_{ES} distributions of B_{tag} candidates. The signal MC are shown on the left and the background MC with the data on the right. The events are required to have one reconstructed neutral B, as well as pass the requirement on the signal lepton momentum. In these plots the signal mode branching fractions are set to 10^{-5}.

effectively suppress such continuum backgrounds, while imposing only a marginal loss in the signal efficiency.

All other particles in the detector, not involved in the B_{tag} reconstruction, are assumed to originate from the B_{signal}. At this point we limit the number of remaining tracks and clusters to six (6) and ten (10) respectively, to reject high-multiplicity topologies, which are clearly inconsistent with signal decays. Stricter requirements on these quantities depend on the particular decay modes considered, and are applied later on in the selection process.

The signal selection requirements specific to each decay mode are discussed in the following section.

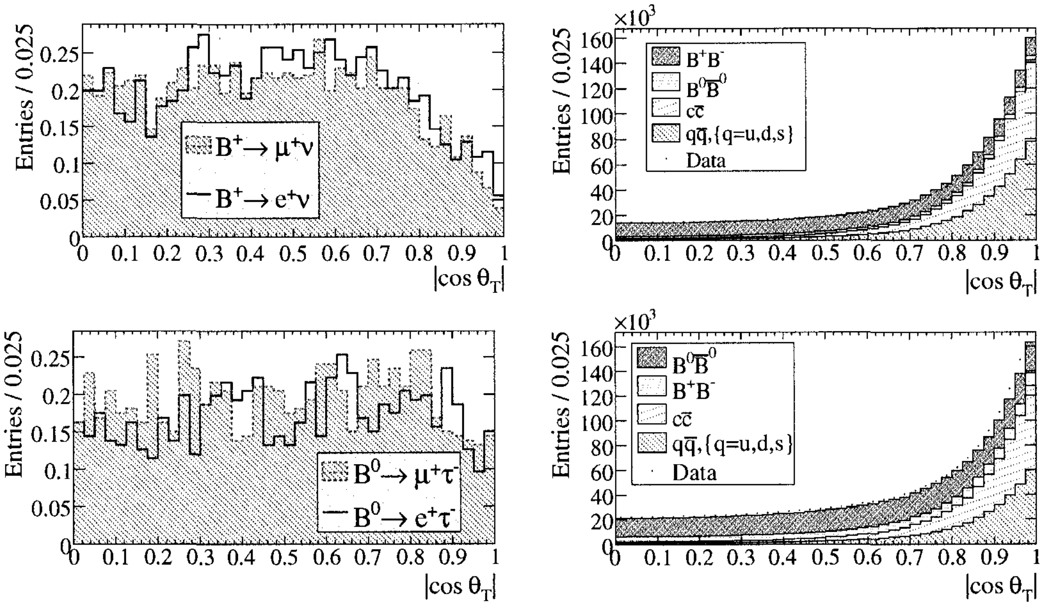

Figure 4–4: Distributions of $|\cos\theta_{\mathrm{T}}|$, cosine of the angle between the calculated thrust axis of the B_{tag} candidate and the thrust axis computed using the signal-side B candidate, for $B^+ \to \ell^+ \nu_\ell$ (top) and $B^0 \to \ell^+ \tau^-$ (bottom). The signal MC are shown on the left and the background MC with the data on the right. The events are required to pass the B_{tag} reconstruction. In these plots the signal mode branching fractions are set to 10^{-5}.

CHAPTER 5
Signal Selection Process

Reconstructing the accompanying B meson (B_{tag}) in specific hadronic modes prior to the signal selection allows the missing momentum vector of the neutrino(s) to be fully determined. The resulting increase in the energy resolution and the ability to infer the B_{signal} rest frame provide the extra kinematic handles which permit signal events to be cleanly distinguished from the background.

Since the $B\bar{B}$ pair's center of mass is known from the beam energy measurements, the reconstruction of the B_{tag} fully determines the B_{signal} 4-vector, by conservation of momentum. In particular for $B^+ \to \ell^+\nu$ and $B^0 \to \ell^+\tau^-$ decays, since the high momentum signal lepton is monoenergetic and is at the kinematic endpoint of the momentum spectrum for B decay, we are provided with a distinctive signature. Figure 4–1 illustrates this process and Figure 5–1 shows a comparison of the lepton momentum distributions in B_{signal} rest frame and the $\Upsilon(4S)$ CM frame. The spread in the lepton momentum distribution in the $\Upsilon(4S)$ CM frame is mainly due to the non-zero momentum of the B_{signal}.

At first we discuss the possible sources of background, and then we will detail the specific signal selection criteria to eliminate such backgrounds.

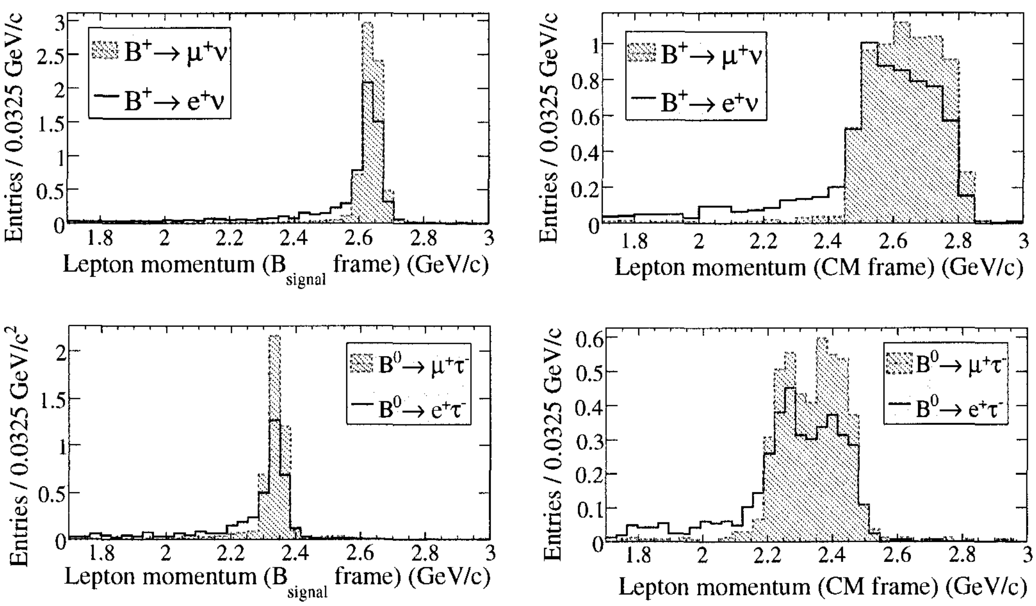

Figure 5–1: The MC distribution of the lepton candidate momentum in the B_{signal} frame and in the $\Upsilon(4S)$ CM frame for $B^+ \to \ell^+ \nu_\ell$ (top) and $B^0 \to \ell^+ \tau^-$ (bottom). The resolution gain provided by the B reconstruction is evident, as a tighter requirement around the peak is possible. In these plots, the branching fractions of $\ell^+ = e^+$ and $\ell^+ = \mu^+$ modes are considered equal.

5.1 Background Processes

Most of the events recorded by the detector are background events and can be categorized as events with either a correctly reconstructed B_{tag}, or a misreconstructed B_{tag}.

The B_{tag} can be misreconstructed from the decay products of $\tau^+\tau^-$ or $q\overline{q}$ ($q = u, d, s, c$) events. Although the B_{tag} reconstruction method suppresses these events significantly, these events can produce a lepton in the same momentum range as the signal. Event shape requirements are used to suppress the background rates further. The B_{tag} can also be misreconstructed from the decay products of $B\overline{B}$ events. For these events the signal lepton candidate can be near the kinematic endpoint, possibly originating from $b \to u\ell\nu_\ell$. Typically one or more particles (pions) has escaped detection in these events, hence requirements on the missing momentum are useful for signal selection.

Out of the $q\overline{q}$ modes, the $c\overline{c}$ mode is expected to be dominant with $\sigma_{c\overline{c}} \approx 1.3$ nb [30]. For this reason, we consider it independently from other $q\overline{q}$ modes (uds). All $q\overline{q}$ backgrounds are expected to be suppressed by the semiexclusive reconstruction, resulting in fewer high momentum particles that could be mistaken as the signal lepton. Similarly, the leptonic continuum background produced in the collider, $e^+ + e^- \to \ell^+\ell^-$ ($\ell = e, \mu, \tau$), is mostly identified and rejected at the reconstruction level. The exceptions are the decays into $\tau^+\tau^-$ (not easily identified, due to the short tau lifetime), which are considered as a possible source of background events. Refer to Table 3–1 for the cross sections of all of these background types, as well as the sizes of the simulated samples.

If the B_{tag} is correctly reconstructed, B_{signal} can still decay in a non-signal mode. The main sources of background from these type of events come from semileptonic events with kinematics closely resembling the signal events. Figure 5–2 illustrates the similarity of the $B^0 \rightarrow \rho^- \ell^+ \nu_\ell$ event with respect to a signal decay. In the case of a high momentum ℓ^+, it is very difficult to discern the kinematics of the identical final state particles between such background and signals (similar scenarios can be constructed for $B^+ \rightarrow \ell^+ \nu_\ell$ modes). Some of these potential background modes are listed in Table 5–1 with their branching fractions. Most of the type $B \rightarrow DX$ are eliminated by vetoing events with any kaons present. The particle identification (PID) criteria are detailed further in later sections. Due to the higher signal lepton momentum, the overall background rate is much lower for the $B^+ \rightarrow \ell^+ \nu_\ell$ modes. However, $B^+ \rightarrow \pi^0 \ell^+ \nu_\ell$ events, where the π^0 has a low energy (or is not reconstructed), contribute. The direction of the missing momentum and the extra energy in the event can be used to eliminate many of these backgrounds.

Other possible background modes for $B^+ \rightarrow \ell^+ \nu_\ell$ are listed in Table 5–2. As such, the branching fractions of these decays are comparable to the signal modes. However, in order to pass the selection criteria, one particle would need to escape detection, and the other to be misidentified. The combined probability of such events occurring makes these modes unlikely to be observed. This is verified by running the MC samples for these modes through a complete signal selection procedure. For example, the ratios of signal ($\mu^+ \nu_\mu$) to background events are calculated to be 195:1 and 38:1 for $K^+ \pi^0$ and $\pi^+ \pi^0$ modes, respectively.

Table 5–1: Other, less likely, $B^0 \rightarrow \ell^+ \tau^-$ backgrounds with their respective branching fractions [3].

Mode	$\mathcal{B}(B^0 \rightarrow ...)$
$B^0 \rightarrow D^{(*)-} \ell^+ \nu_\ell (\gamma)$	$7.47 \pm 0.28 \times 10^{-2}$
$B^0 \rightarrow D^{(*)-} \pi^+$	$3.4 \pm 0.9 \times 10^{-3}$
$B^0 \rightarrow \rho^- \ell^+ \nu_\ell$	$2.3 \pm 0.4 \times 10^{-4}$
$B^0 \rightarrow \pi^- \ell^+ \nu_\ell$	$1.36 \pm 0.15 \times 10^{-4}$

Table 5–2: Other, less likely, $B^+ \rightarrow \ell^+ \nu_\ell$ backgrounds with their respective branching fractions [3].

Mode	$\mathcal{B}(B^+ \rightarrow ...)$
$B^+ \rightarrow \pi^+ \pi^0$	$(5.5 \pm 0.6) \times 10^{-6}$
$B^+ \rightarrow K^0 \pi^+$	$(2.41 \pm 0.17) \times 10^{-5}$
$B^+ \rightarrow K^+ \pi^0$	$(1.21 \pm 0.08) \times 10^{-5}$
$B^+ \rightarrow e^+ \nu_e \gamma$	$< 2.0 \times 10^{-4}$
$B^+ \rightarrow \mu^+ \nu_\mu \gamma$	$< 5.2 \times 10^{-5}$

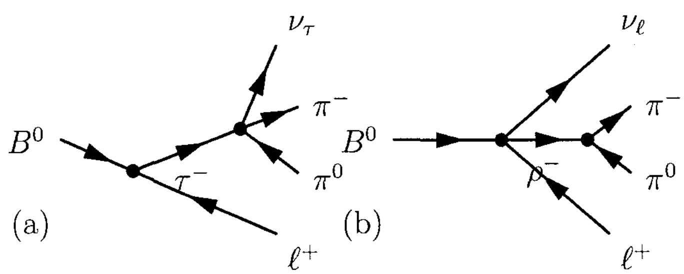

Figure 5–2: An example of (a) signal event, (b) background event with identical final state particles.

5.2 Signal Selection

The quantities considered in the signal selection are listed below and discussed in more detail in the following sections.

Signal Lepton Requirements:

- track momentum in the B_{signal} frame (the signal lepton candidate),
- particle identification for the signal lepton candidate (either e or μ),
- veto events with kaons,

Tau Reconstruction Requirements:

- reconstructed τ mass and charge,
- τ daughter candidate momenta in τ rest frame.

Additional Selection Requirements:

- track and cluster multiplicities,
- direction and magnitude of the missing momentum in the event,
- extra energy in the event,

5.2.1 Signal Lepton Selection

The B_{tag} reconstruction allows us to determine the rest frame of the B_{signal}, providing distinct signatures for the two body decay signal events. In the B_{signal} frame the primary leptons (ℓ_1) have the momenta of $\sim 2.63\,\text{GeV}$ for $B^+ \to \ell^+\nu_\mu$ and $\sim 2.34\,\text{GeV}/c$ for $B^0 \to \ell^+\tau^-$. Initially, we look for a high momentum track between 1.7 and 3.0 GeV that passes the PID criteria for either an electron or a muon. This momentum requirement is left loose in order to create a large sideband region, which will be used to determine the background PDF shape and normalization. The signal yield is ultimately extracted from a maximum likelihood fit to the signal lepton momentum. The signal regions are defined to be 2.40-2.75 GeV for $B^+ \to \ell^+\nu_\mu$ and 2.20-2.42 GeV for $B^0 \to \ell^+\tau^-$. The signal and background momentum distributions are shown in Figure 5–3. Figure 5–4 shows the signal MC distributions for the lepton momentum, fitted with a Crystal Ball function [37]. The tail, especially visible for $\ell^+ = e^+$ modes, is mostly due to unreconstructed bremsstrahlung photons. As the signal region includes some of this tail, the numbers for background events in the signal region are misleadingly elevated. The maximum likelihood fitting procedure, however, takes into account the sharply peaking nature of the signal distribution.

The muon PID criteria are kept loose to partly compensate for the lower overall efficiency of muon identification. The muon PID is based on neural network selection which considers the energy deposited into EMC, the average value and the uncertainty in the number of hit strips per layer, the average value and the uncertainty in number of interaction lengths of detector material traversed by the track, as well as the χ^2 on the track candidate relating to the fitting of the track trajectory to the IFR detector activity. The electron PID is based on likelihood selection, which takes into account the energy deposited into EMC, the lateral shape of showers in the EMC, the Cherenkov angle in the DIRC, as well as the dE/dx measurement in the DCH and SVT. In addition to the track PID requirement, any events with an identified kaon are vetoed, since these are most likely $B \to DX$ decays (visible as a small bump in the p^* distributions around 2.25 GeV, Figure 5–3).

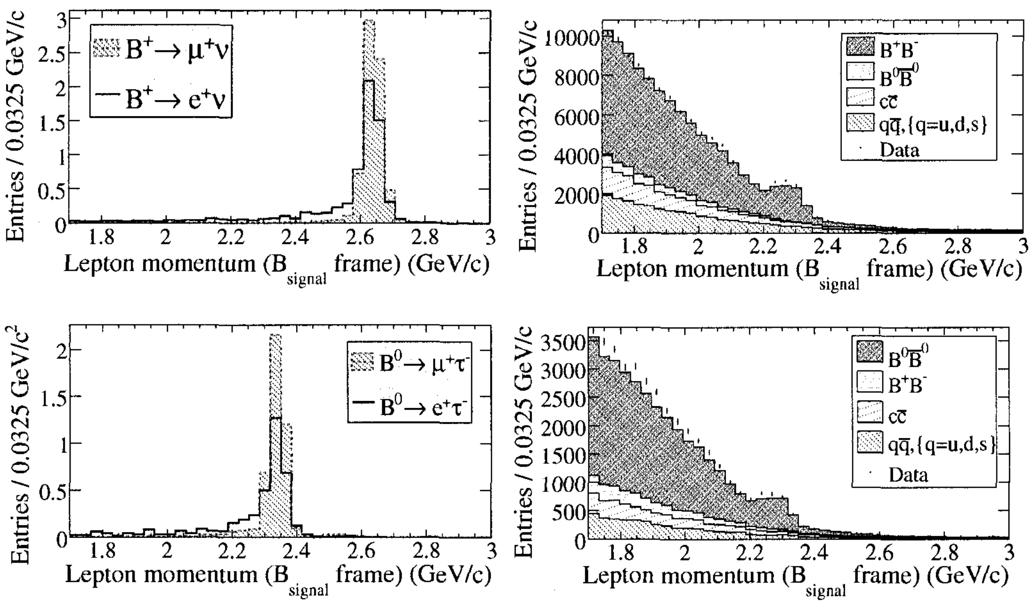

Figure 5–3: Distributions of p^*, the signal lepton momentum in the B_{signal} frame, for $B^+ \longrightarrow \ell^+ \nu_\mu$ (top) and $B^0 \longrightarrow \ell^+ \tau^-$ (bottom). The events are required to pass B_{tag} reconstruction. The signal MC are shown on the left and the background MC with the data on the right. The discrepancy between the data and MC at the low momenta is mostly due to poorly modeled combinatorial contribution, and disappears after more of the signal selection criteria is applied. In these plots the signal mode branching fractions are set to 10^{-5}.

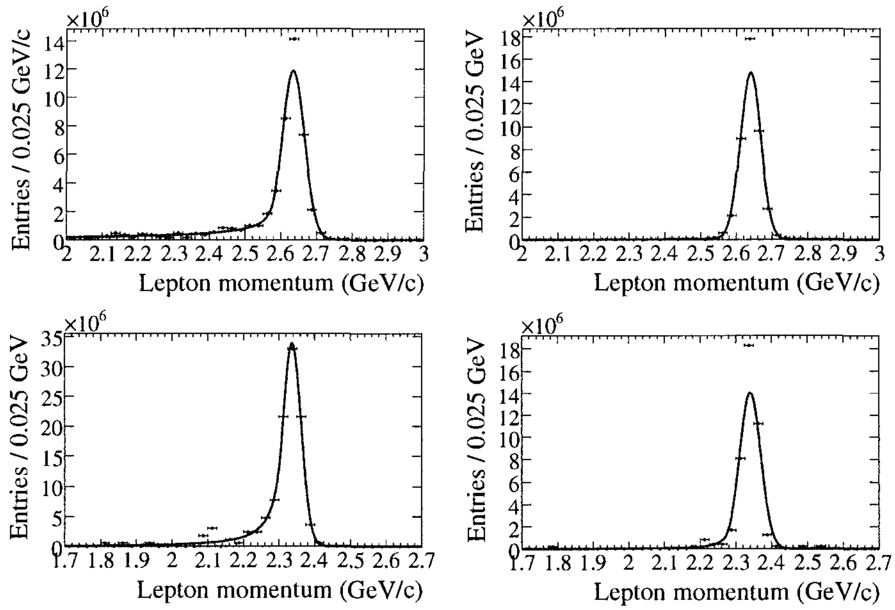

Figure 5–4: Distributions of p^* signal MC for $B^+ \to e^+ \, \nu_e$ and $B^+ \to \mu^+ \, \nu_\mu$ (top, left and right), and $B^0 \to e^+ \, \tau^-$ and $B^0 \to \mu^+ \, \tau^-$ (bottom, left and right). The events are required to pass the B_{tag} reconstruction, as well as the PID on the lepton candidate.

5.2.2 τ Reconstruction Requirements

In the $B^0 \to \ell^+\tau^-$ decays, the signal decay to a τ and the accompanying lepton ℓ_1 (e or μ) is a two body process, allowing us to determine the τ rest frame by observing the recoil of the accompanying lepton around the B_{signal}.

The τ^- rest frame is calculated from the observed signal lepton, assuming the nominal energy and momentum of the τ^- for a 2-body B^0 decay (E_τ=2.937 GeV, p_τ=2.34 GeV/c). The six τ decay modes considered are listed in Table 5–3. The second highest momentum track in the event (excluding B_{tag} reconstruction) is assumed to be a τ daughter, and is required to have a charge opposite to the primary signal lepton. If this track satisfies electron or muon PID, the event is considered to be a leptonic τ decay. Otherwise, the track is assumed to be a pion and a quantity ΔE_τ is calculated for all other τ decay modes according to

$$\Delta E_\tau = \sum_i E_{\pi_i} + p_\nu - m_\tau, \tag{5.1}$$

where the sum is over the τ daughter candidates, the momentum of the neutrino is $p_\nu = |\sum \vec{p}_{\pi^-,\pi^0}|$, $m_\tau = 1.777\,\text{GeV}$ [3] and all quantities are measured in the τ^- rest frame. The charged pions originating from the τ^- decay are demanded to satisfy likelihood selection criteria, which takes into account the energy deposited into EMC, the Cherenkov angle in the DIRC, as well as the dE/dx measurement in the DCH and SVT. Neutral pions are reconstructed from two clusters ($\pi^0 \to \gamma\gamma$) by adding their 4-vectors. The clusters are also required to have an energy of at least 20 MeV in the CM frame. The invariant mass of the π^0 is required to fall in the range 0.115-0.150 GeV. The ΔE_τ distributions are shown in Figure 5–5. The tail below zero, present for the default decay mode, $\tau^- \rightarrow \pi^- \nu_\tau$, is due to events where one or more particles were not reconstructed properly or escaped the geometric acceptance of the detector. The required values for each decay mode are listed in Table 5–4.

Table 5–3: The τ decays that are considered, with their branching fractions (in %) [3].

τ decay mode	Branching Fraction
$\tau^- \rightarrow e^- \overline{\nu}_e \nu_\tau$	17.84±0.05
$\tau^- \rightarrow \mu^- \overline{\nu}_\mu \nu_\tau$	17.36±0.05
$\tau^- \rightarrow \pi^- \nu_\tau$	10.90±0.07
$\tau^- \rightarrow \pi^- \pi^0 \nu_\tau$	25.50±0.10
$\tau^- \rightarrow \pi^- \pi^0 \pi^0 \nu_\tau$	9.25±0.12
$\tau^- \rightarrow \pi^- \pi^- \pi^+ \nu_\tau$	9.33±0.08

For each event, we assign the decay mode for which $|\Delta E_\tau|$ is smallest, requiring additional conditions for the decay modes that proceed through the intermediate resonances $\rho^- \rightarrow \pi^-\pi^0$, $a_1{}^- \rightarrow \pi^-\pi^0\pi^0$ and $a_1{}^- \rightarrow \pi^-\pi^-\pi^+$. We calculate a quantity

$$\cos\theta_{\tau-\rho} = \frac{2E_\tau E_\rho - m_\tau^2 - m_\rho^2}{2|\vec{p_\tau}||\vec{p_\rho}|}, \tag{5.2}$$

where $(E_\tau, \vec{p_\tau})$ and $(E_\rho, \vec{p_\rho})$ are the four-momenta in the B_{signal} frame, m_τ and m_ρ are the masses of the τ and ρ respectively. For a correctly reconstructed ρ, this quantity peaks near unity. If the candidate does not satisfy $\cos\theta_{\tau-\rho} > 0.70$ the mode with the next smallest $|\Delta E_\tau|$ (if one is present) is selected instead. Analogous quantities are calculated for $\tau^- \rightarrow \pi^- \pi^0 \pi^0 \nu_\tau$ and $\tau^- \rightarrow \pi^- \pi^- \pi^+ \nu_\tau$ modes, but with an $a_1^\pm$ instead of a $\rho^\pm$. The requirements of $\cos\theta_{\tau-a_1} > 0.45$ and $\cos\theta_{\tau-a_1} > 0.35$ are used for the two cases, respectively. We demand no additional requirements on ρ or a_1. The signal and background distributions are shown in Figure 5–6.

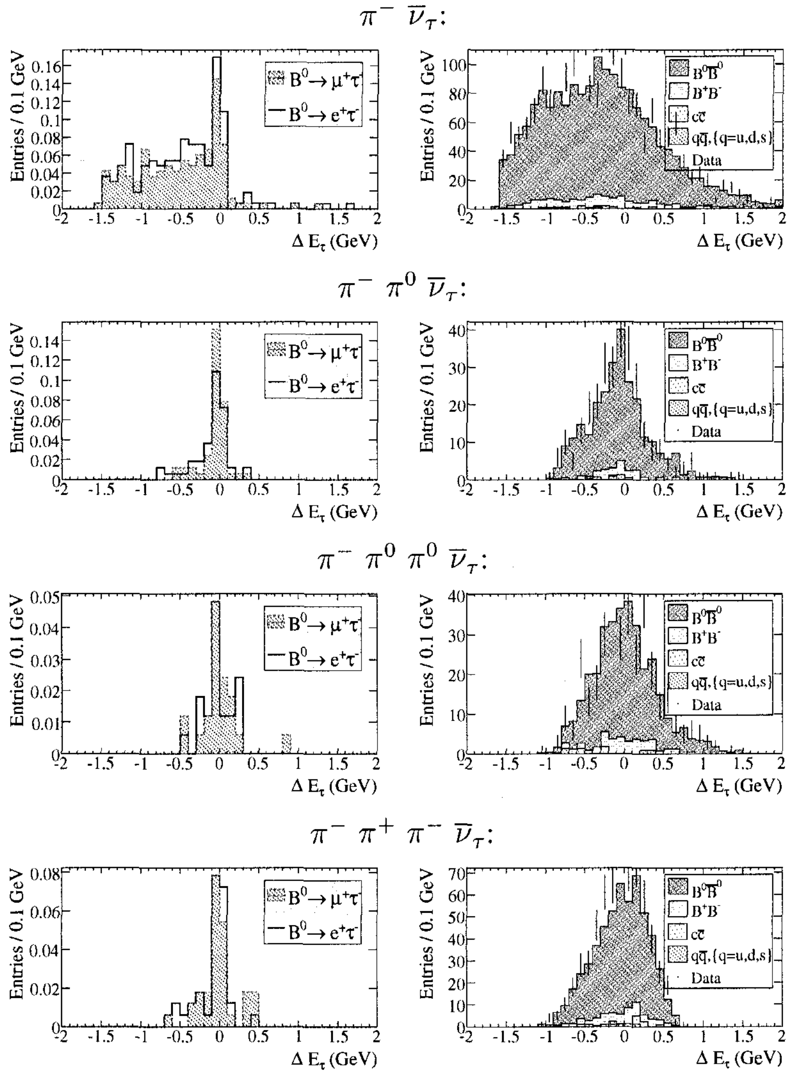

Figure 5–5: The distributions of ΔE_τ for the semileptonic τ decay modes. The signal MC are shown on the left and the background MC with the data on the right. The events are required to pass the B_{tag} reconstruction and the signal lepton selection requirements, as well as the correct τ charge requirement. In these plots the signal mode branching fractions are set to 10^{-5}.

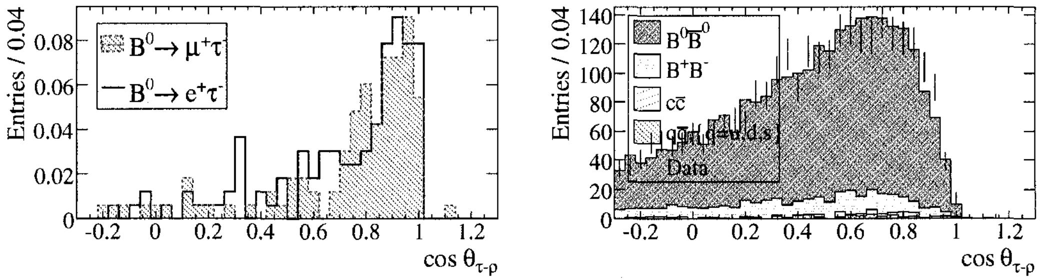

Figure 5–6: The distributions of $\cos\theta_{\tau-\rho}$. The signal MC are shown on the left and the background MC with the data on the right. The events are required to pass the B_{tag} reconstruction, the signal lepton selection requirements, as well as the correct τ charge requirement. In these plots the signal mode branching fractions are set to 10^{-5}.

5.2.3 Additional Selection Requirements

The multiplicities of neutral clusters and charged tracks in the signal side are shown in Figures 5–7 and 5–8. The selection requirements on the multiplicities depend on the τ decay mode, and are listed in Table 5–4. In general, we allow for two extra charged tracks and six extra neutral clusters in the signal side. This allows for a presence of low energy particles in the detector not (necessarily) associated with the decay of the $\Upsilon(4S)$. The requirement on the extra energy in the event is utilized further on to make sure that such particles indeed are unimportant for the analysis.

Since neutrinos escape detection, a corresponding amount of "missing momentum" is present for signal events. Thanks to the reconstruction method, the magnitude and direction of this quantity are well determined, and can be calculated according to

$$\vec{p^*}_{\text{miss}} = \vec{p^*}_{\Upsilon(4S)} - \vec{p^*}_{B_{\text{tag}}} - \sum_i \vec{p^*}_i, \tag{5.3}$$

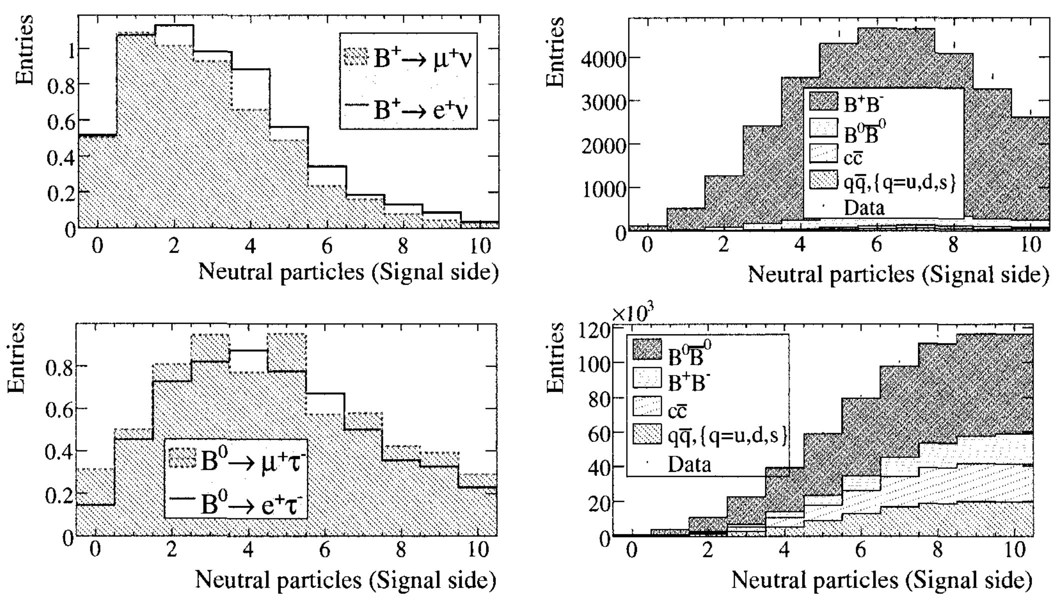

Figure 5–7: The distributions of cluster multiplicities in each event. The signal MC are shown on the left and the background MC with the data on the right. The events are required to pass the $B_{\rm tag}$ reconstruction and the signal lepton selection requirements. In these plots the signal mode branching fractions are set to 10^{-5}.

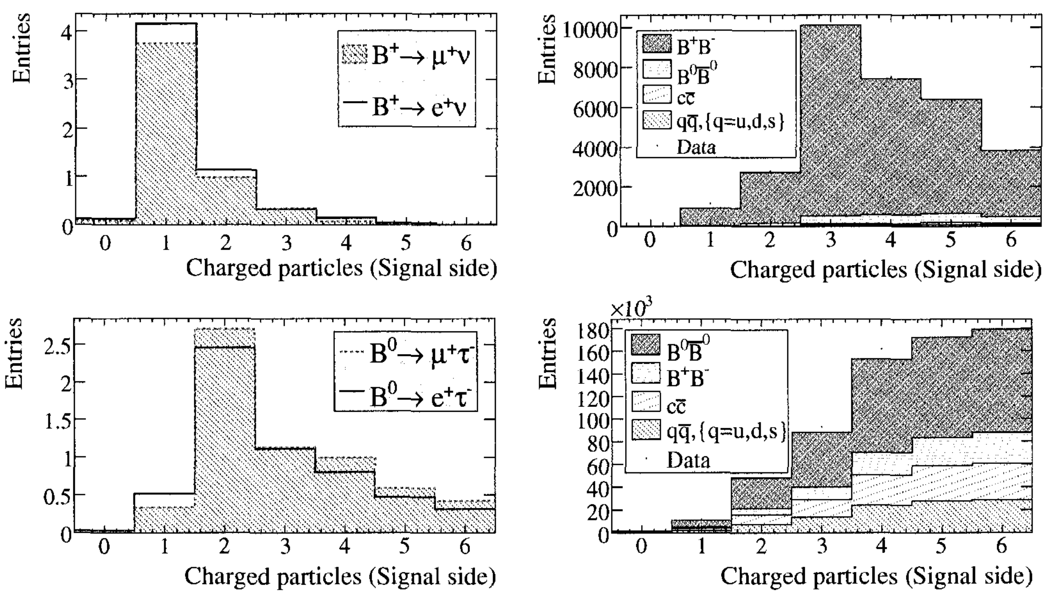

Figure 5–8: The distributions of charged track multiplicities in each event. The signal MC are shown on the left and the background MC with the data on the right. The events are required to pass the B_{tag} reconstruction and the signal lepton selection requirements. In these plots the signal mode branching fractions are set to 10^{-5}.

where the sum goes over the particles not associated with the reconstruction of the B_{tag}. The missing momentum is calculated in the B_{signal} rest frame for $B^+ \to \ell^+ \nu_\ell$ modes, and in the τ rest frame for $B^0 \to \ell^+ \tau^-$ modes.

The extra momentum in the event, ΔP_{miss}, is calculated according to

$$\Delta P_{\text{miss}} = |\vec{p}_{\text{miss}} + \sum \vec{p}_{\pi,l}|, \tag{5.4}$$

where $p_{\pi,l}$ are the momenta of the charged lepton or the pions (from the τ decay). By requiring ΔP_{miss} to be close to zero, only events where the missing momentum (as carried by the neutrino(s)) opposes the rest of the signal particles are accepted. The signal selection criteria for this variable are shown in Table 5–4. The distributions are shown in Figures 5–10 and 5–11.

For $B^+ \to \ell^+ \nu_\ell$ modes we also calculate a quantity describing the direction of the missing momentum, $\cos\theta_{p_{\text{miss}}}$:

$$\cos\theta_{p_{\text{miss}}} = p_{z\,\text{miss}}/p_{\text{miss}}, \tag{5.5}$$

where the subscript z indicates the component of the momentum in the direction parallel to the beam pipe, as measured in the $\Upsilon(4S)$ CM frame. The acceptable range for this variable are determined by the geometry of the detector; events outside of the geometrical acceptance of the detector are excluded. This is done to ensure that the missing momentum is carried by the neutrino, and not a particle that could have been detected if the detector had full angular coverage. The distributions for this variable are shown in Figure 5–9. We select events with $-0.76 < \cos\theta_{p_{\text{miss}}} < 0.92$, where the values are determined by the geometric acceptance of the detector.

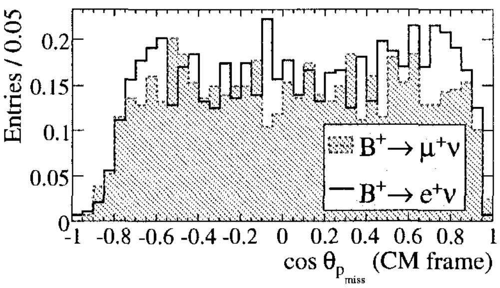

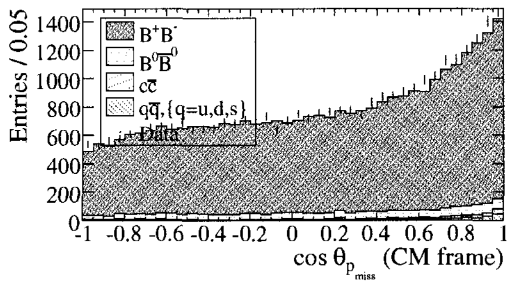

Figure 5–9: The distribution of $\cos\theta_{p_{\text{miss}}}$, cosine of the angle of the total event missing momentum vector with respect to the beam pipe. The signal MC are shown on the left and the background MC with the data on the right. The events are required to pass the B_{tag} reconstruction and the signal lepton selection requirements. In these plots the signal mode branching fractions are set to 10^{-5}.

The above requirements are complemented by another limitation on the extra energy in the system:

$$E_{\text{extra}} = \sum_i E_{\text{i}^{\text{th}}\text{track}} + \sum_i E_{\text{i}^{\text{th}}\text{cluster}} - E_{l_1} - \sum_i E_{\pi_i, l_2}, \tag{5.6}$$

where all energies are measured in the CM frame. E_{extra} therefore describes the amount of energy recorded by the detector, but not accounted for by the high momentum lepton and the τ daughters. The clusters and tracks associated with the reconstruction of B_{tag} are excluded from the sums, and only clusters with energy more than 50 MeV in the CM frame are considered. The signal selection criteria for this variable are shown in Table 5–4. The distributions are shown in Figures 5–12 and 5–13.

The signal efficiencies after each signal selection requirement are listed in Tables 5–5 and 5–6. The signal selection efficiencies for each of the τ decay modes are listed in Tables 5–7 and 5–8. Tables 5–9 and 5–10 show the marginal efficiencies for

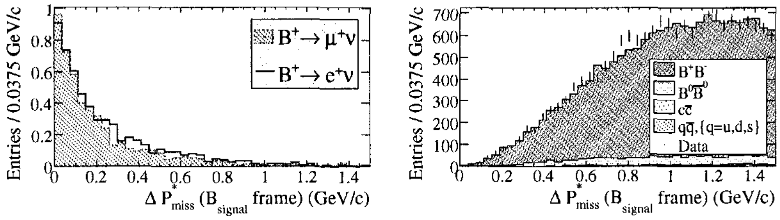

Figure 5–10: The distributions of ΔP_{miss} for $B^+ \to \ell^+ \, \nu_\ell$. The signal MC are shown on the left and the background MC with the data on the right. The events are required to pass the B_{tag} reconstruction and the signal lepton requirements. In these plots the signal mode branching fractions are set to 10^{-5}.

each signal selection requirement (marginal efficiency is the efficiency of a given requirement, had it been applied after all other requirements). The background event counts and efficiencies, as the signal selection requirements are applied, can be found in Tables 5–11, 5–12, 5–13 and 5–14.

In addition to the signal selection presented above, quantities such as the missing mass or the reconstructed τ daughters' momenta (Figures 5–14 and 5–15 respectively) could be considered in future studies. However, in order to maximize the signal selection efficiency, we apply no selection criteria on these quantities.

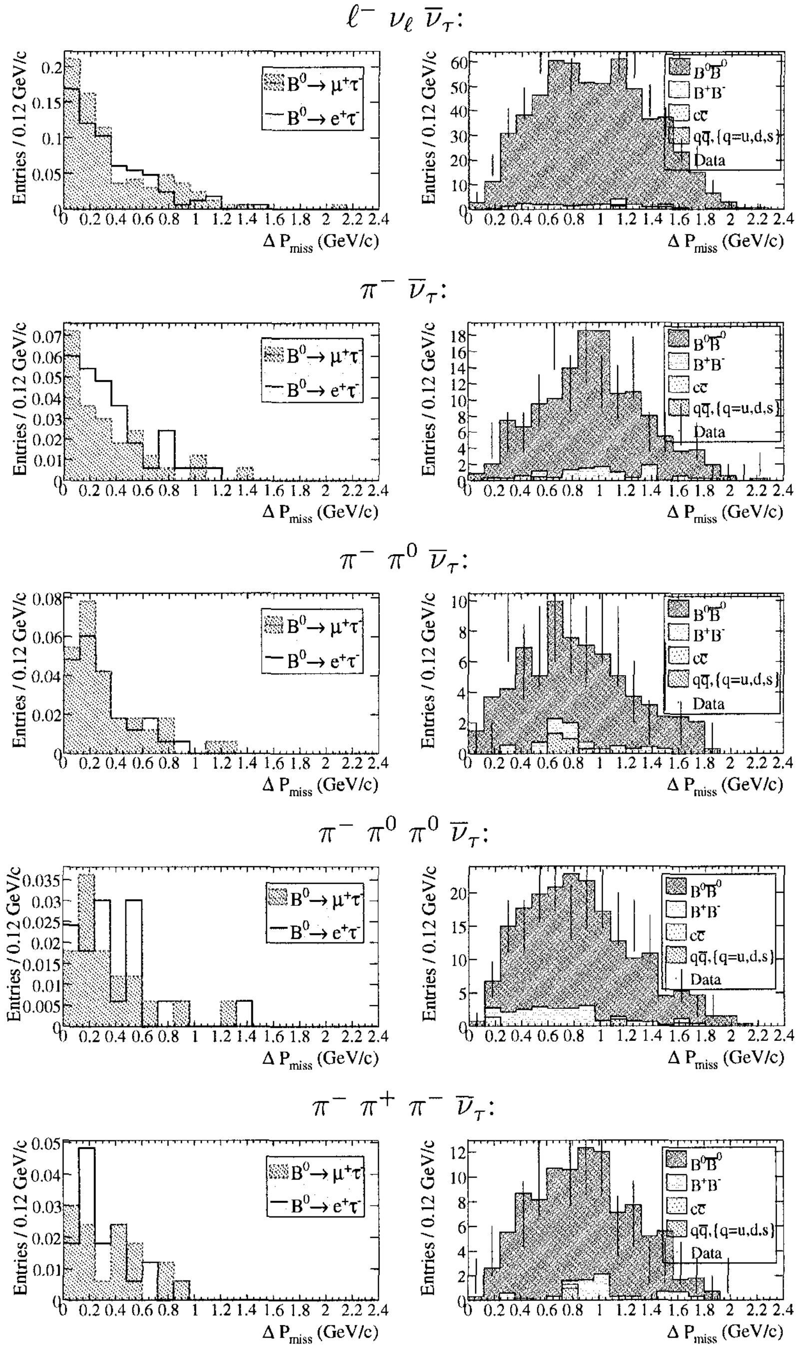

Figure 5–11: The distributions of ΔP_{miss} for $B^0 \to \ell^+ \, \tau^-$, for each τ decay mode. The signal MC are shown on the left and the background MC with the data on the right. The events are required to pass the B_{tag} reconstruction, signal lepton requirements, as well as the τ reconstruction criteria. In these plots the signal mode branching fractions are set to 10^{-5}.

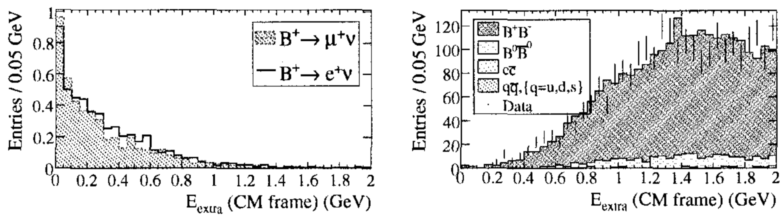

Figure 5–12: The distributions of E_{extra} for $B^+ \to \ell^+ \nu_\ell$, for each τ decay mode. The signal MC are shown on the left and the background MC with the data on the right. The events are required to pass B_{tag} reconstruction and the signal lepton requirements In these plots the signal mode branching fractions are set to 10^{-5}.

Table 5–4: The signal selection criteria for each decay mode. The energies (momenta) are in GeV (GeV/c).

Mode	Cut					
	ΔE_τ	ΔP_{miss}	E_{extra}	p_{l,π,ρ,a_1}	N_{trk}	N_{clus}
$B^0 \to \ell^+ \tau^-$						
$e^+ \nu \overline{\nu}$	n/a	< 1.2	< 0.6	0.15-0.95	2-4	< 6
$\mu^+ \nu \overline{\nu}$	n/a	< 1.2	< 0.6	0.15-0.95	2-4	< 6
$\pi^+ \overline{\nu}$	-0.10-0.06	< 0.8	< 0.6	0.8-0.92	2-4	< 6
$\pi^+ \pi^0 \overline{\nu}$	-0.14-0.06	< 0.9	< 0.6	0.5-0.82	2-4	< 8
$\pi^+ \pi^0 \pi^0 \overline{\nu}$	-0.3-0.3	< 1.0	< 0.7	0.2-0.82	2-4	< 10
$\pi^+ \pi^- \pi^0 \overline{\nu}$	-0.1-0.1	< 1.0	< 0.75	0.3-0.82	4-6	< 6
$B^+ \to \ell^+ \nu$	n/a	< 0.7	< 1.2	n/a	1-6	< 10

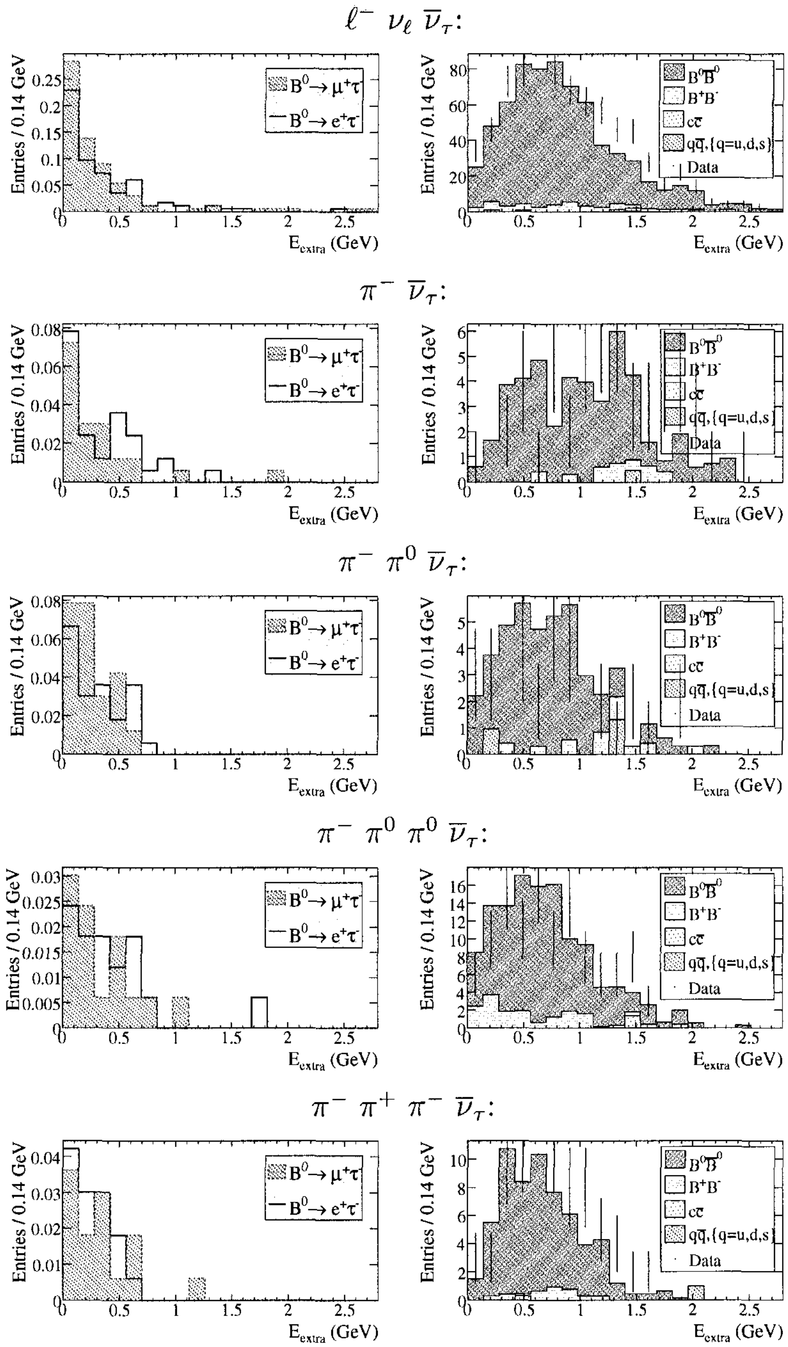

Figure 5–13: The distributions of E_{extra} for $B^0 \to \ell^+ \tau^-$, for each τ decay mode. The signal MC are shown on the left and the background MC with the data on the right. The events are required to pass B_{tag} reconstruction, signal lepton requirements, as well as the τ reconstruction criteria. In these plots the signal mode branching fractions are set to 10^{-5}.

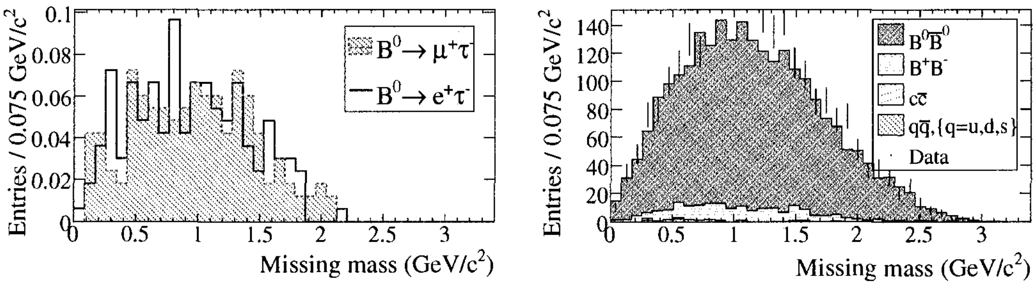

Figure 5–14: The distributions of the missing mass for the various τ decay modes. The signal MC are shown on the left and the background MC with the data on the right. The events are required to pass the B_{tag} reconstruction, the signal lepton selection requirements, as well as the τ reconstruction criteria (charge and ΔE_τ). In these plots the signal mode branching fractions are set to 10^{-5}. This quantity is not used in signal selection at this time.

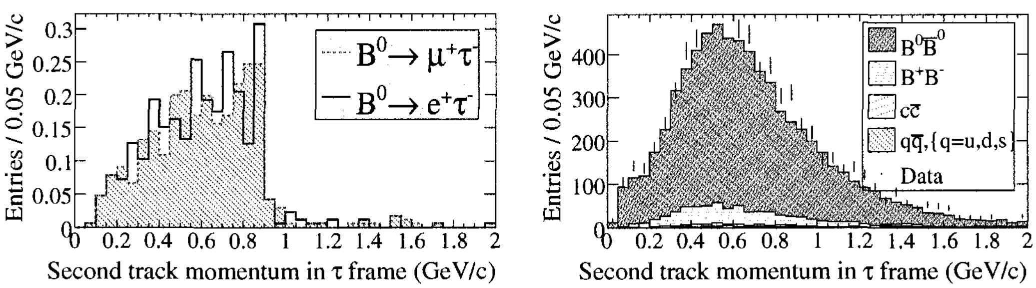

Figure 5–15: The distributions of the charged τ daughter candidate's momentum in the τ frame. The signal MC are shown on the left and the background MC with the data on the right. The events are required to pass the B_{tag} reconstruction, the signal lepton selection requirements, as well as the correct τ daughter charge requirement. In these plots the signal mode branching fractions are set to 10^{-5}. This quantity is not used in signal selection at this time.

Table 5–5: Efficiencies (in %) for $B^+ \to \ell^+\nu_\ell$ signal Monte Carlo, after each consecutive selection requirement is applied.

Cut	Signal Monte Carlo $B^+ \to \mu^+\nu_\mu$ (1329)	Signal Monte Carlo $B^+ \to e^+\nu_\mu$ (2803)
Charged B	0.212±0.005	0.223±0.005
m_{ES}	0.201±0.004	0.212±0.005
$\cos\theta_{\mathrm{T}}$	0.192±0.004	0.199±0.005
Lepton momentum	0.182±0.004	0.163±0.005
PID	0.139±0.004	0.148±0.004
Track charge	0.136±0.004	0.146±0.004
$\cos\theta_{p_{\mathrm{miss}}}$	0.130±0.003	0.140±0.003
ΔP_{miss}	0.121±0.003	0.132±0.003
E_{extra}	0.120±0.003	0.131±0.003

Table 5–6: Efficiencies (in %) for $B^0 \to \ell^+\tau^-$ signal Monte Carlo, after each consecutive selection requirement is applied. These efficiencies include all τ decay modes.

Cut	Signal Monte Carlo $B^0 \to \mu^+\tau^-$	Signal Monte Carlo $B^0 \to e^+\tau^-$
Neutral B	0.273±0.007	0.306±0.007
m_{ES}	0.178±0.005	0.183±0.005
$\cos\theta_{\mathrm{T}}$	0.164±0.005	0.171±0.005
Lepton momentum	0.110±0.004	0.095±0.004
PID	0.081±0.004	0.086±0.004
Multiplicities	0.077±0.005	0.083±0.004
τ charge	0.067±0.003	0.072±0.003
ΔE_τ	0.033±0.002	0.039±0.002
ΔP_{miss}	0.032±0.002	0.037±0.002
E_{extra}	0.028±0.002	0.033±0.002
Daughter momentum	0.026±0.002	0.030±0.002

Table 5–7: $B^0 \to e^+\tau^-$ signal selection efficiencies (in %) for each τ decay mode. The selection efficiency is the fraction of events that pass through all of the selection criteria. "Signal Side" efficiency represents the fraction of events passing the selection after a successful $B_{\rm tag}$ reconstruction. "τ reco" efficiency represents the fraction of events passing the selection after a correctly charged τ candidate has been identified.

Mode	Selection (%)	After B Reconstruction (%)	τ reco (%)
$e^+\nu\overline{\nu}$	0.0075±0.0011	4.5±0.6	11.9±1.9
$\mu^+\nu\overline{\nu}$	0.0039±0.0008	2.1±0.4	5.7±1.4
$\pi^+\ \overline{\nu}$	0.0053±0.0009	3.0±0.5	7.9±1.6
$\pi^+\ \pi^0\ \overline{\nu}$	0.0044±0.0008	2.5±0.4	6.7±1.4
$\pi^+\ \pi^0\ \pi^0\ \overline{\nu}$	0.0025±0.0007	1.5±0.3	4.0±1.0
$\pi^+\ \pi^-\ \pi^+\ \overline{\nu}$	0.0030±0.0007	1.7±0.4	4.5±1.3
Total	0.0264±0.0020	15.3±1.1	40.6±3.6

Table 5–8: $B^0 \to \mu^+\tau^-$ signal selection efficiencies (in %) for each τ decay mode. The selection efficiency is the fraction of events that pass through all of the selection criteria. "Signal Side" efficiency represents the fraction of events passing the selection after a successful $B_{\rm tag}$ reconstruction. "τ reco" efficiency represents the fraction of events passing the selection after a correctly charged τ candidate has been identified.

Mode	Selection (%)	After B Reconstruction (%)	τ reco (%)
$e^+\nu\overline{\nu}$	0.0095±0.0013	5.5±0.6	13.9±1.9
$\mu^+\nu\overline{\nu}$	0.0053±0.0010	3.2±0.5	8.2±1.4
$\pi^+\ \overline{\nu}$	0.0044±0.0009	2.5±0.4	6.4±1.1
$\pi^+\ \pi^0\ \overline{\nu}$	0.0060±0.0010	3.6±0.5	9.0±1.5
$\pi^+\ \pi^0\ \pi^0\ \overline{\nu}$	0.0022±0.0006	1.4±0.3	3.5±0.9
$\pi^+\ \pi^-\ \pi^+\ \overline{\nu}$	0.0030±0.0007	1.8±0.4	4.6±1.1
Total	0.0304±0.0023	18.0±1.1	45.8±3.3

Table 5–9: The marginal efficiencies of the selection requirements for both the signal and background Monte-Carlo for $B^+ \to \ell^+ \nu_\ell$ modes. This value is the efficiency of the requirement, had it been applied after all other requirements. The efficiencies are expressed in percent (%) for the signal modes, and as fractions for the background modes.

Cut	$B^+ \to e^+ \nu_\ell$	$B^+ \to \mu^+ \nu_\mu$	B^+B^-	$B^0\overline{B}^0$	Rest of MC
m_{ES}	97.2±0.5	97.3±0.4	25/28	0/2	0/4
$\cos\theta_{\mathrm{T}}$	96.7±0.5	96.0±0.5	25/29	0/0	0/0
E_{extra}	99.0±0.3	97.8±0.4	25/30	0/1	0/0
ΔP_{miss}	95.4±0.6	96.6±0.5	25/34	0/1	0/0
PID	79.5±1.0	93.5±0.7	25/65	0/1	0/13
Lepton momentum	99.1±0.3	89.4±0.8	25/8325	0/808	0/88

Table 5–10: The marginal efficiencies of the selection requirements for both the signal and background Monte-Carlo for $B^0 \to \ell^+ \tau^-$ modes. This value is the efficiency of the requirement, had it been applied after all other requirements. The efficiencies are expressed in percent (%) for the signal modes, and as fractions for the background modes.

Cut	$B^0 \to \mu^+ \tau^-$	$B^0 \to e^+ \tau^-$	$B^0\overline{B}^0$	Rest of MC
E_{extra}	94.5±1.6	91.5±2.3	20/34	0/1
ΔP_{miss}	98.4±0.9	97.2±1.4	20/22	0/4
PID	70.6±2.8	93.3±2.0	20/209	0/32
Lepton momentum	91.3±1.9	79.1±3.1	20/741	0/48
Multiplicities	96.4±1.3	95.2±1.8	20/22	0/0
Daughter momentum	99.5±0.5	97.2±1.4	20/22	0/1
ΔE_τ	81.6±3.6	85.6±3.7	16/27	0/1

Table 5–11: $B^+ \rightarrow \ell^+ \nu_\ell$ background event counts for background Monte Carlo after each consecutive selection requirement is applied. The $B\overline{B}$ samples are almost three times the size of the data sample. The raw number of simulated events for each background type can be seen in Table 3–1.

Cut	Background type			
	B^+B^-	$B^0\overline{B}^0$	$c\bar{c}$	uds
Charged B	3218230 ± 1789	1275220 ± 1128	2989930 ± 1725	2444810 ± 1561
m_{ES}	1509380 ± 1227	267834 ± 517	549628 ± 741	458948 ± 677
$\cos\theta_{\mathrm{T}}$	1333930 ± 1154	225794 ± 475	$269461 pm 518$	222351 ± 471
Track p^*	5422 ± 74	762 ± 27	1614 ± 40	1688 ± 41
PID	266 ± 16	7 ± 3	11 ± 3	17 ± 4
Track Q	238 ± 15	5 ± 2	9 ± 3	8 ± 3
$\cos\theta_{p_{\mathrm{miss}}}$	207 ± 14	5 ± 2	9 ± 3	4 ± 2
ΔP_{miss}	30 ± 5	1 ± 1	7 ± 3	0
E_{extra}	25 ± 5	0	0	0
w/ e ID	17 ± 4	0	0	0
w/ μ ID	8 ± 3	0	0	0

Table 5–12: Event counts for $B^+ \rightarrow \ell^+ \nu_\ell$ background Monte Carlo after each consecutive selection requirement is applied, normalized to the total data luminosity.

Cut	Background type			
	B^+B^-	$B^0\overline{B}^0$	$c\bar{c}$	uds
Charged B	1038334 ± 579	411438 ± 364	2180290 ± 1261	2466445 ± 1577
m_{ES}	486988 ± 396	86414 ± 166	400795 ± 541	463009 ± 683
$\cos\theta_{\mathrm{T}}$	430381 ± 372	72851 ± 153	$196494 pm 379$	224319 ± 476
Track p^*	1749 ± 23	245 ± 8.9	1177 ± 29	1703 ± 41
PID	85.8 ± 5.3	2.3 ± 0.9	8.0 ± 2.4	17.2 ± 4.2
Track Q	76.8 ± 5.0	1.6 ± 0.7	6.6 ± 2.2	8.1 ± 2.9
$\cos\theta_{p_{\mathrm{miss}}}$	66.8 ± 4.64	1.6 ± 0.7	6.6 ± 2.2	4.0 ± 2.0
ΔP_{miss}	9.7 ± 1.8	1.0 ± 0.6	5.1 ± 1.9	0
E_{extra}	8.1 ± 1.6	0.3 ± 0.3	0	0
w/ μ ID	5.5 ± 1.3	0	0	0
w/ e ID	2.6 ± 0.9	0	0	0

Table 5–13: $B^0 \to \ell^+ \tau^-$ background event counts for background Monte Carlo after each consecutive selection requirement is applied. The $B\overline{B}$ samples are almost three times the size of the data sample. The raw number of simulated events for each background type can be seen in Table 3–1. The $\tau^+\tau^-$ backgrounds are negligible.

Cut	Background type			
	B^0B^0	B^+B^-	$c\bar{c}$	uds
Neutral B	2169590 ± 1470	1031140 ± 1015	1554820 ± 1245	1017660 ± 1008
$m_{\rm ES}$	922581 ± 960	214973 ± 464	284602 ± 533	194223 ± 441
$\cos\theta_{\rm T}$	810024 ± 899	181711 ± 426	140703 ± 375	95590 ± 309
Track p^*	145898 ± 381	21523 ± 146	4843 ± 69	2413 ± 49
PID	846 ± 29	92 ± 10	13 ± 4	12 ± 3
τ charge	646 ± 11	70 ± 8	10 ± 3	4 ± 2
ΔE_τ	165 ± 6	19 ± 4	2 ± 1	0
$\Delta P_{\rm miss}$	154 ± 5	18 ± 4	2 ± 1	0
$E_{\rm extra}$	76 ± 4	10 ± 3	2 ± 1	0
2^{nd} Track p	60 ± 4	10 ± 3	2 ± 1	0
w/ μ ID	37 ± 6	5 ± 2	1 ± 1	0
w/ e ID	22 ± 5	5 ± 2	1 ± 1	0

Table 5–14: Event counts for $B^0 \to \ell^+ \tau^-$ background Monte Carlo after each consecutive selection requirement is applied, normalized to the total data luminosity. The values include all decay modes; the composition of the background events can be seen in more detail in Table 5–17. The $\tau^+\tau^-$ backgrounds are negligible.

Cut	Background type			
	$B^0\overline{B}^0$	B^+B^-	$c\bar{c}$	uds
Neutral B	699999 ± 475	332688 ± 740	1133791 ± 909	1026666 ± 1017
m_{ES}	297662 ± 310	156760 ± 338	207534 ± 389	195941 ± 445
$\cos\theta_{\text{T}}$	261347 ± 290	132505 ± 310	102602 ± 273	96435 ± 312
Track p^*	47072 ± 123	15694 ± 107	3531 ± 50	2434 ± 50
PID	273.0 ± 9.4	67.1 ± 7.0	9.5 ± 2.6	12.1 ± 3.5
τ charge	208.4 ± 8.2	51.0 ± 6.1	7.3 ± 2.3	4.0 ± 2.0
ΔE_τ	53.2 ± 4.1	13.9 ± 3.2	1.5 ± 1.0	0
ΔP_{miss}	49.7 ± 4.0	13.1 ± 3.1	1.5 ± 1.0	0
E_{extra}	24.5 ± 2.8	7.3 ± 2.3	1.5 ± 1.0	0
2^{nd} Track p	19.4 ± 2.4	7.3 ± 2.3	0.7 ± 0.7	0
w/ μ ID	11.9±2.0	3.7±1.6	0.7 ± 0.7	0
w/ e ID	7.1±1.5	3.7±1.6	0.7 ± 0.7	0

Table 5–15: Event counts for $B^+ \to \ell^+ \nu_\ell$ data and MC (normalized to the total onpeak luminosity) after each consecutive selection requirement is applied. The values include all decay modes.

Cut	Background type	
	Data	MC total
Charged B	5806080 ± 2391	6097346 ± 2469
m_{ES}	1375400 ± 1170	1437356 ± 1199
$\cos\theta_{\text{T}}$	887105 ± 940	924140 ± 961
Track momentum	4741 ± 68	4877 ± 69
Lepton PID	118 ± 11	113.3 ± 10.6
Track charge	104 ± 10	93.1 ± 9.6
$\cos\theta_{p_{\text{miss}}}$	85 ± 9	79.0 ± 8.9
ΔP_{miss}	12 ± 4	15.8 ± 4.0
E_{extra}	9 ± 3	8.4 ± 2.9

Table 5–16: Event counts for $B^0 \to \ell^+ \tau^-$ data and MC (normalized to the total onpeak luminosity) after each consecutive selection requirement is applied. The values include all decay modes.

Cut	Background type	
	Data	MC total
Neutral B	3070340 ± 1745	2893486 ± 1701
m_{ES}	751098 ± 866	857968 ± 926
$\cos\theta_{\mathrm{T}}$	511820 ± 715	592931 ± 770
Track momentum	365 ± 19	361.7 ± 19.0
Lepton PID	264 ± 16	270.7 ± 16.4
τ charge	54 ± 7	68.6 ± 8.3
ΔE_τ	35 ± 6	33.3 ± 5.8
ΔP_{miss}	22 ± 4.7	26.7 ± 5.2
E_{extra}	18 ± 4.2	16.3 ± 4.0

Table 5–17: The $B^0 \to \ell^+ \tau^-$ background counts ("cut and count" method) normalized to the onpeak data luminosity. The errors quoted are purely statistical.

Mode	$B^0 \to e^+\tau^-$	$B^0 \to \mu^+\tau^-$
$e^+\nu\overline{\nu}$	0.31±0.31	0
$\mu^+\nu\overline{\nu}$	0	0.30±0.30
$\pi^+\overline{\nu}$	0.60±0.43	0.31±0.31
$\pi^+\pi^0\overline{\nu}$	0.30±0.30	1.16±0.82
$\pi^+\pi^0\pi^0\overline{\nu}$	0.63±0.45	0.31±0.31
$\pi^+\pi^-\pi^+\overline{\nu}$	0.31±0.31	0.92±0.65
Total	2.16±0.93	3.00±1.17

5.3 Sideband Regions

The *sideband* regions are used for further studies of the background events, as well as for MC-data comparisons. Since these regions are defined to be just outside of the signal regions, they are expected to have minimal sensitivity to the signal modes, but contain background events which are similar to those expected in the signal region. The various sideband regions considered are

- The the B_{tag} m_{ES} sideband, between 5.22 and 5.30 GeV/c^2,
- ΔE_τ sidebands, between -0.2 and 0.2 GeV, but excluding the signal region,
- lepton p^* sideband, between 1.7 and 2.8 GeV/c, but excluding the signal region,
- $36.1 fb^{-1}$ of *offpeak* data, approximately 40 MeV below the *onpeak* CM energy.

The offpeak data is used to test the signal selection sensitivity to continuum events. As the B_{tag} reconstruction and the lepton momentum criteria alone are able to suppress the continuum background to zero, no further studies are possible. This can be viewed as a consistency check, since if any events survived, it would indicate a problem. In order to verify the expected absence of other combinatorial events (e.g. misreconstructed $B\overline{B}$ events) in the signal region we study the m_{ES} sideband, while applying the signal selection requirements sequentially. Figures 5–16 and 5–17 show the evolution of the m_{ES} distribution as more of the signal selection requirements are applied. The continuum contribution is greatly suppressed after the initial lepton momentum requirement, and the combinatorial $B\overline{B}$ events are virtually eliminated by PID and track/cluster multiplicity requirements. The surviving background events are primarily semileptonic decays from a B_{tag} of correct charge. Figures 5–18 and 5–19 show ΔE_τ plotted against p^* for the signal MC and the data after all other signal selection requirements have been applied. The remaining events in the p^* sidebands are useful for normalizing the fitting background PDFs to the data luminosity, as explained in the next section.

5.4 Estimating Backgrounds

The background estimate can be extracted by counting the number of background events in the MC that survive the signal selection, and normalizing the result

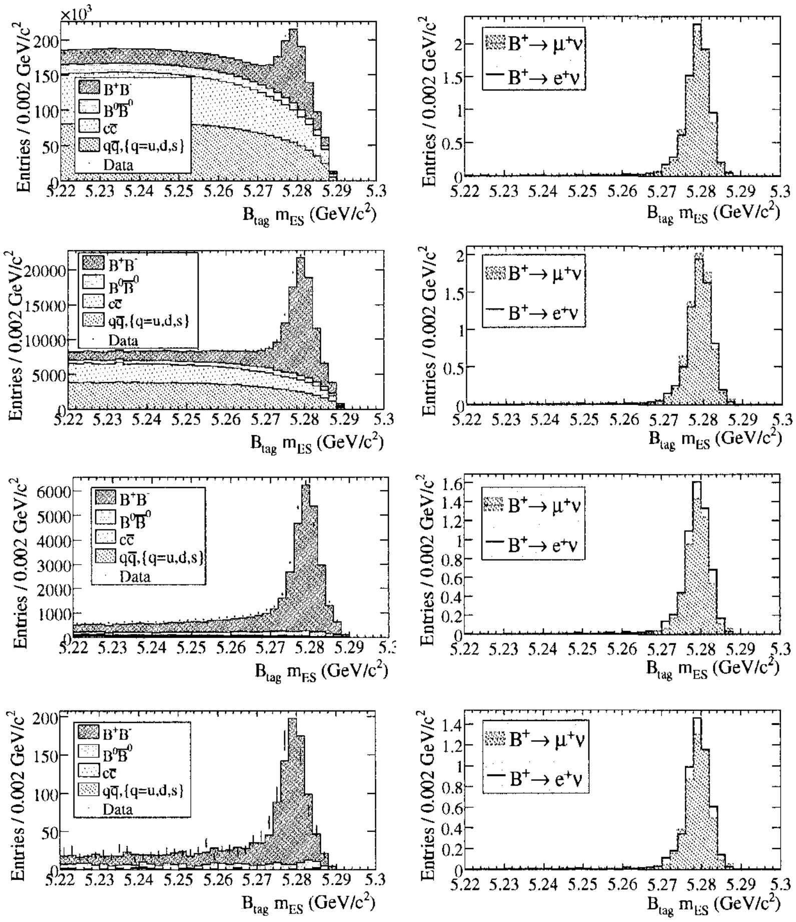

Figure 5–16: $B^+ \to \ell^+ \; \nu_\ell \; m_{\rm ES}$ distributions after $B_{\rm tag}$ charge requirement (top), with additional (loose) lepton momentum requirements, with PID and multiplicity requirements, and with $E_{\rm extra}$ and $\Delta P_{\rm miss}$ requirements (bottom). The signal MC are shown on the left and the background MC with the data on the right.

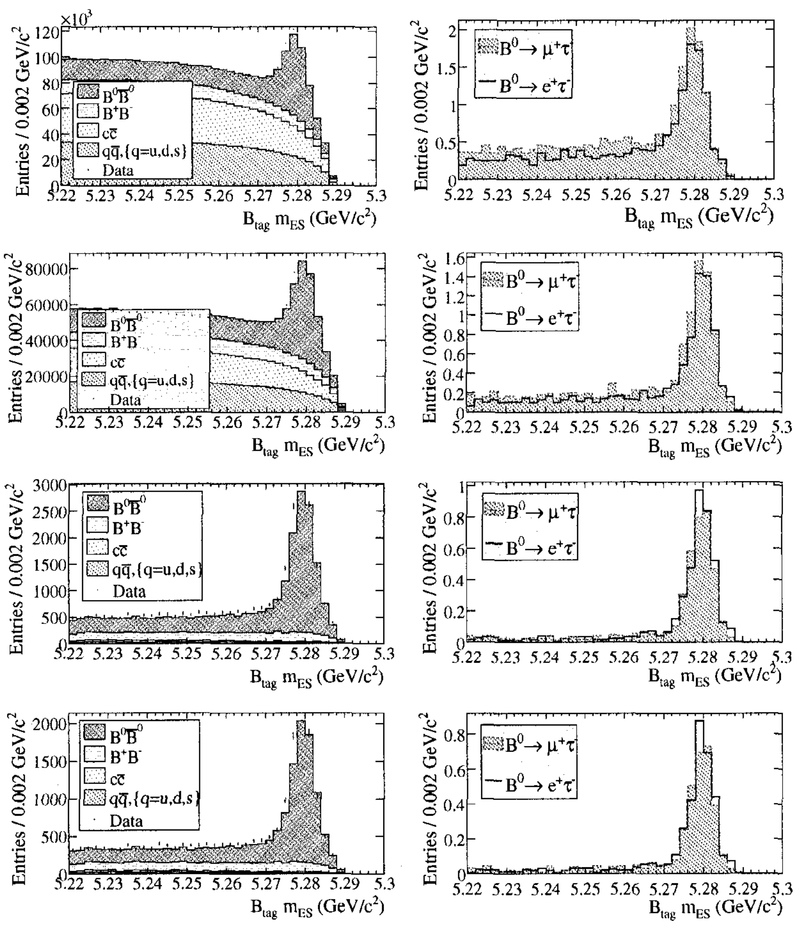

Figure 5–17: $B^0 \rightarrow \ell^+\ \tau^-\ m_{\mathrm{ES}}$ distributions after B_{tag} charge requirement (top), with additional (loose) lepton momentum requirements, with PID and multiplicity requirements, and with E_{extra} and ΔP_{miss} requirements (bottom). The signal MC are shown on the left and the background MC with the data on the right.

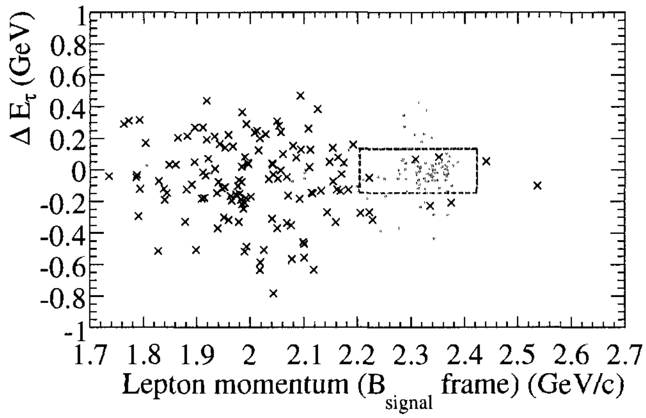

Figure 5–18: ΔE_τ versus p^*, after all other selection criteria have been applied. The solid dots are $B^0 \to e^+\tau^-$ signal MC events (excluding $\tau^- \to \ell^-\nu\nu$ decay modes) and the crosses are data events. The approximate location of the signal region (decay mode dependent) is shown as the box in the middle.

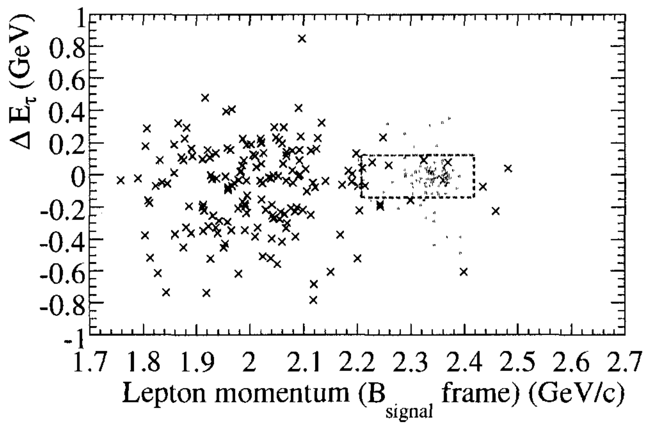

Figure 5–19: ΔE_τ versus p^*, after all other selection criteria have been applied. The solid dots are $B^0 \to \mu^+\tau^-$ signal MC events (excluding $\tau^- \to \ell^-\nu\nu$ decay modes) and the crosses are data events. The approximate location of the signal region (decay mode dependent) is shown as the box in the middle.

to the data luminosity. However, for analyses with very few events, low statistics are prone to introduce high uncertainties in such estimates. As an alternative to the "cut and count" approach, we proceed to extract the background estimate utilizing a fit to the ℓ_1 p^* distributions. For $B^0 \to \ell^+ \tau^-$ modes we are presented with an option to consider each of the τ decay modes separately. Although the signal lepton momentum distribution for the signal events is ideally independent of the τ reconstruction, it is not so for the background events, where the event kinematics may bias the τ reconstruction. This prevents us from assuming a universal shape for the background fitting function. Due to the low statistics present in each of the τ-decay modes, we choose to fit all τ-decay modes together, reducing the uncertainties in the fitting parameters.

The signal and background MC distributions are fitted by phenomenological probability density functions (PDF). The signal distributions are modeled with Crystal Ball functions to account for the energy loss due to unreconstructed bremsstrahlung photons. The $B^+ \to \ell^+\nu$ background is modeled with an exponential decay and a Gaussian distribution, while the $B^0 \to \ell^+ \tau^-$ background is modeled with a double Gaussian distribution.

Figure 5–20 shows the fits of the background PDFs to the background MC. The flatness of the distributions near the signal region makes the extracted results (number of events in the signal box) only loosely dependent on the choice of PDF. The uncertainties in these estimates are obtained by generating additional toy MC samples based on the signal and background PDFs, with statistics equivalent to the MC samples. Each of these samples is then fitted using the same method as the original MC sample, allowing us to determine the expected statistical fluctuations in PDF parameters due to the fitting procedure.

The number of expected background events is extracted by integrating the fit PDFs over the blinding region. The blinding region is the range in the p^* where we expect the signal events to be found from (the sharply peaking component in the signal p^* distribution). The data events in the blinding region are kept hidden [1] (blind) in order to avoid bias in the analysis procedure. Only after the analysis procedure has been finalized, are the data looked at in their entirety. The fitting procedure is then repeated for the blinded data (see Figure 5–21). The number of events obtained from the MC and data are listed in Table 5–18, along with the result of the "cut and count" approach. The MC and data background estimates are all consistent with each other, with the values extracted from fits having smaller uncertainties.

Table 5–18: Number of background events in the blinding region, extracted from the generic MC and the data.

Method	Signal mode			
	$B^+ \to e^+\nu$	$B^+ \to \mu^+\nu$	$B^0 \to e^+\tau^-$	$B^0 \to \mu^+\tau^-$
MC fit	0.52 ± 0.16	0.89 ± 0.36	2.22 ± 0.23	3.01 ± 0.34
Data fit	0.51 ± 0.22	0.61 ± 0.39	2.52 ± 0.32	3.09 ± 0.38
MC "cut and count"	0.45 ± 0.32	0.72 ± 0.51	2.48 ± 0.94	3.93 ± 1.13

[1] Any event that passes the signal requirement for p^* is removed from the data sample.

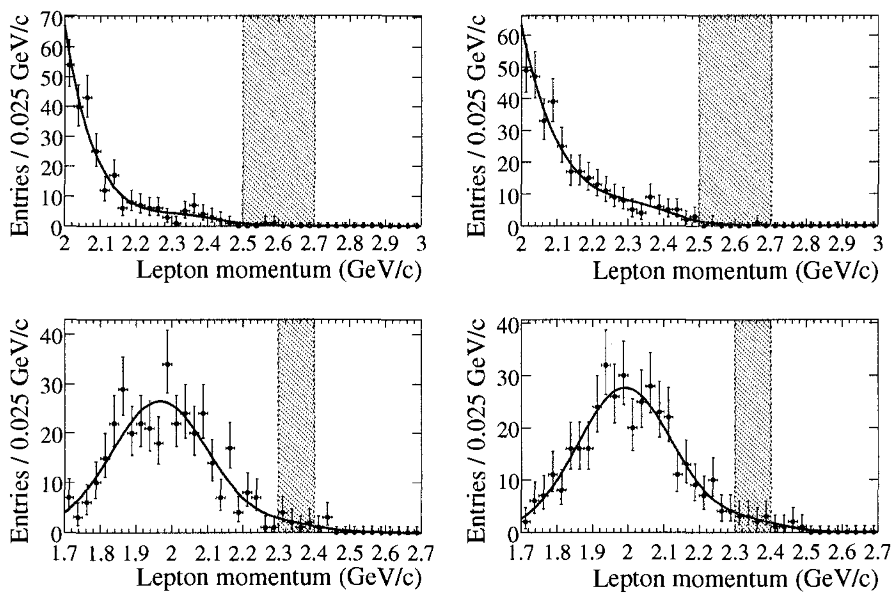

Figure 5–20: The background MC distributions for the signal lepton momentum are fitted for $B^+ \rightarrow e^+ \nu_e$ and $B^+ \rightarrow \mu^+ \nu_\mu$ (top left and right), and $B^0 \rightarrow e^+ \tau^-$ and $B^0 \rightarrow \mu^+ \tau^-$ (bottom left and right). The dashed box represents the location of the blinding region.

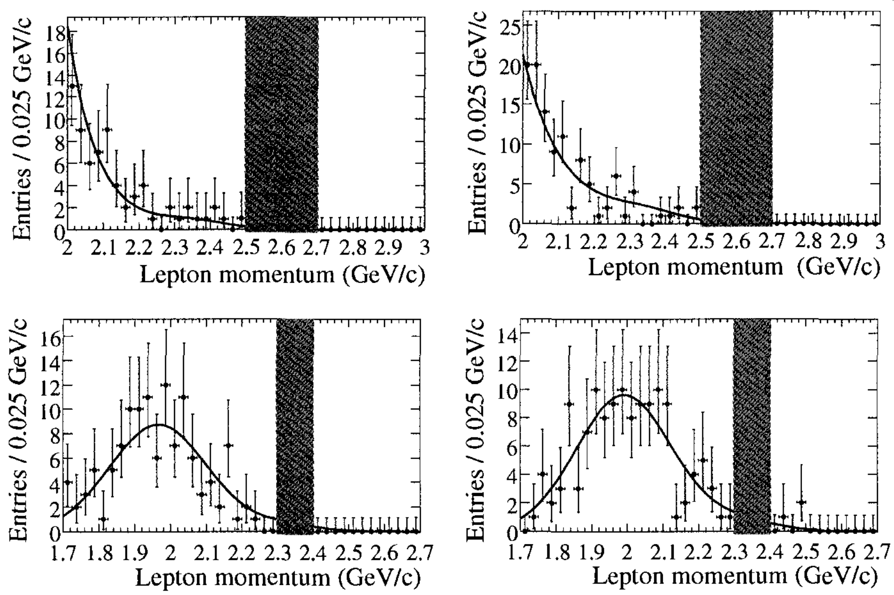

Figure 5–21: The data distributions for the signal lepton momentum are fitted for $B^+ \rightarrow e^+ \ \nu_e$ and $B^+ \rightarrow \mu^+ \ \nu_\mu$ (top left and right), and $B^0 \rightarrow e^+ \ \tau^-$ and $B^0 \rightarrow \mu^+ \ \tau^-$ (bottom left and right). The dashed box represents the location of the blinding region.

5.5 Extracting the results

The signal yields are extracted from unbinned maximum likelihood fits to the signal lepton momentum distributions, as measured in the B_{signal} frame, where the PDF shape parameters are determined from the MC samples. The fit is done using the following likelihood function:

$$\mathcal{L}(n_s, n_b) = \frac{e^{-(n_s+n_b)}}{N!} \prod_{i=1}^{N} (n_s f_s(i) + n_b f_b(i)), \tag{5.7}$$

where N is the total number of events in the fit region, $f_s(i)$ and $f_b(i)$ are the PDFs for the signal and background, n_b and n_s are the number of background and signal events. All parameters of the signal and background PDFs remain fixed, while n_s and n_b are allowed to float. The fits are done over ranges in p^* shown in Figure 5–22. The number of signal events given by the fits are consistent with zero for all decay modes.

The 90% confidence level upper limit on the branching fraction, $\mathcal{B}$, is determined by solving for $\mathcal{B}^{90\%}$ in:

$$0.90 = \int_0^{\mathcal{B}^{90\%}} \mathcal{L}(\mathcal{B}) d\mathcal{B} / \int_0^{\infty} \mathcal{L}(\mathcal{B}) d\mathcal{B}, \tag{5.8}$$

for events lying in the signal regions of $2.40\,\text{GeV}/c < p^* < 2.75\,\text{GeV}/c$ for $B^+ \to \ell^+\nu$ and $2.20\,\text{GeV}/c < p^* < 2.42\,\text{GeV}/c$ for $B^0 \to \ell^+\tau^-$ (n_s^* and n_b^*). The branching fraction, $\mathcal{B}$, is related to the likelihood through a substitution $n_s^* = \epsilon_{\text{tot}} \times 2 \times N_{\text{tag}} \times \mathcal{B}$, where ϵ_{tot} is the total signal selection efficiency and N_{tag} is the total number of B^+B^- or $B^0\overline{B}^0$ pairs (depending on the decay mode) in the data sample. The following

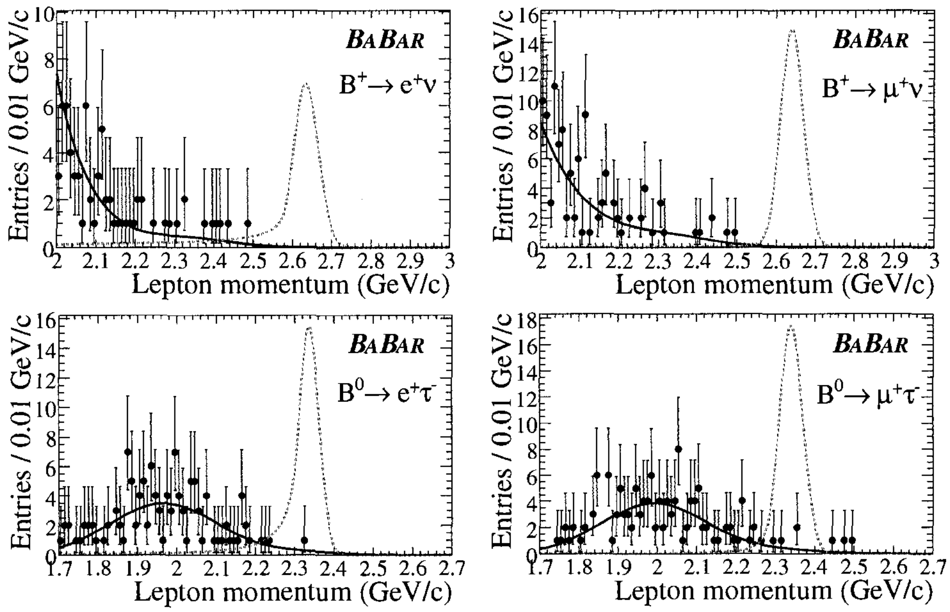

Figure 5–22: The unbinned maximum likelihood fits on the lepton momentum in data. The dashed line, representing the signal PDF with an arbitrary scaling, indicates where the signal is expected.

Chapter discusses the systematic effects and uncertainties involved in the analysis procedure.

CHAPTER 6
Uncertainties

The MC and data are compared to estimate possible systematic effects that might affect the analysis results. To take such effects into account, systematic uncertainties are estimated for some of the quantities derived from the MC samples. Whenever two uncertainties are quoted, the first is statistical and the second is systematic.

An uncertainty in the tracking algorithm is considered to introduce an additional 0.8%/trk additive systematic uncertainty per signal track[1] (e.g. 1.6% for $B^0 \to \ell^+\tau^-$, $\tau^- \to \pi\nu$, which contains two charged tracks).

The PID efficiencies are estimated according to the standard *BABAR* procedures, using data control samples based on $\tau^+\tau^-$ decays, radiative Bhabba events and dimuon events. We find the MC samples to overestimate the efficiencies in the data. Table 6–1 shows the approximate correction factors, to be applied to the MC, for various particle types and momentum ranges. Since the exact efficiencies vary run by run, a global average is quoted. The specific correction factors and the associated systematic uncertainties depend on the given decay mode. The misidentification rate of leptons as pions is also studied, and is found to have no significant effect.

[1] This is a standard *BABAR* procedure [39]

Table 6–1: The scaling corrections needed to compensate for the differing PID efficiencies between data and MC (Data/MC).

	PID < 1 GeV	PID 2-3 GeV
Electrons	0.97 ± 0.01	1.00 ± 0.01
Muons	0.95 ± 0.02	0.98 ± 0.02
Charged Pions	0.98 ± 0.01	-
Neutral Pions	0.96 ± 0.06	-

The cross-feed between the various τ decay modes is approximately 15% between modes with pions. The leptonic modes, as well as $\tau \to \pi^-\pi^-\pi^+$, are reconstructed very cleanly (less than 5% cross-feed). In general, the signal events with a wrong decay mode tag tend to have ΔE_τ less than zero, indicating a low momentum τ daughter having escaped detection. Since the statistical uncertainty in the number of signal events in each mode ranges from 20% to 30%, we do not consider additional corrections to compensate for the mode mixing. Moreover, since we consider all τ decay modes together in the fitting method, any systematic effects present will have no effect on the number of extracted signal events.

The $B\overline{B}$ yields (number of $B\overline{B}$ events in the $m_{\rm ES}$ signal region) are studied for MC and data. We find the MC to slightly underestimate this quantity for both charged and neutral $B\overline{B}$ pairs. Figure 6–1 shows the $m_{\rm ES}$ distributions for MC and data, which are fitted with a combination of ARGUS [38] and a Crystal Ball functions. The number of $m_{\rm ES}$ peaking events is estimated by integrating the peaking component between 5.270 and 5.288 GeV. The yield corrections are calculated on samples with $\cos\theta_T$ and particle multiplicity requirements applied, since we find that the $m_{\rm ES}$ sidebands are otherwise modeled poorly. We refrain from applying more selection requirements in order to retain the maximum statistics possible. The $B\overline{B}$ yield corrections are estimated for charged and neutral $B\overline{B}$ pairs independently.

There are two major sources of uncertainties affecting this scaling correction factor. One arises from the shape of the ARGUS component, which describes the background contribution due to combinatorial events. We proceed to switch the ARGUS shapes between the MC and data fits, and redo the rest of the fitting procedure. While the actual $B\overline{B}$ yields vary significantly depending on the choice of ARGUS shape, there is very little variation in the ratio of Data to MC yields. The results of these fits are listed in Table 6–2.

Table 6–2: The ratios of Data and MC (Data/MC) for m_{ES} peaking events, using various ARGUS PDF shapes. The uncertainties are statistical.

	fixed PDFs (MC)	fixed PDFs (Data)	free PDFs
$B^0\overline{B}^0$	1.06 ± 0.04	1.05 ± 0.04	1.10 ± 0.04
B^+B^-	1.05 ± 0.03	1.04 ± 0.03	1.05 ± 0.03

The second source of uncertainty comes from the fact that while $B\overline{B}$ yield correction affects the signal efficiency, it is estimated from a generic $B\overline{B}$ sample which has obvious differences in the particle multiplicities and kinematics, compared to a signal event. While applying more selection requirements makes the remaining events resemble signal events more, doing so decreases the statistics of the sample greatly. We study this effect by fitting the m_{ES} distributions at various stages of the signal selection: after B_{tag} selection, with the $\cos\theta_T$ requirement, and with particle multiplicity requirements. The resulting $B\overline{B}$ scaling correction factors are listed in Table 6–3.

According to the observed variations in the yield correction due to above sources, we assign a systematic uncertainty of 0.05 to the $B\overline{B}$ yield scaling correction factors. Thus, the $B\overline{B}$ yield scaling correction factors are determined to be $1.11 \pm 0.04 \pm 0.05$ and $1.05 \pm 0.03 \pm 0.05$ for $B^0\overline{B}^0$ and B^+B^- respectively. The scaling corrections have an effect on the signal selection efficiency, obtained from the signal MC. Since the background is estimated through a fit to the data, there are no scaling corrections that need to be applied to it.

Table 6–3: The ratios of Data and MC (Data/MC) for m_{ES} peaking events, for different stages of the signal selection. The uncertainties are statistical.

	B_{tag}	after $\cos\theta_T$	after multiplicity requirements
$B^0\overline{B}^0$	1.13 ± 0.02	1.11 ± 0.03	1.10 ± 0.04
B^+B^-	1.14 ± 0.02	1.10 ± 0.03	1.05 ± 0.03

In order to study the behavior of the p^* fits, we proceed to generate toy MC samples. Figure 6–2 shows the p^* fits on generated samples with varying number of signal events, but background fixed to the actual background yield in the data. The likelihood plots, as functions of the branching fraction assumption, are also shown.

Possible bias in the fitting procedure is studied by generating additional toy MC samples according to the background and signal PDFs, varying the number of generated signal events. Table 6–4 shows the average values (over 100 trials) for the number of signal events in the fit region (N_{sig}) and the likelihood calculation region (n_{s}). The quoted uncertainties are obtained from the widths of the distributions. Figure 6–3 show the bias ($N_{\mathrm{gen}} - N_{\mathrm{sig}}$) as a function of the number of generated signal events. The error bars on these plots are the uncertainties on the mean. The pull, $(N_{\mathrm{gen}} - N_{\mathrm{sig}})/\sigma_{\mathrm{fit}}$, is shown in Figure 6–4. The shapes are consistent with a

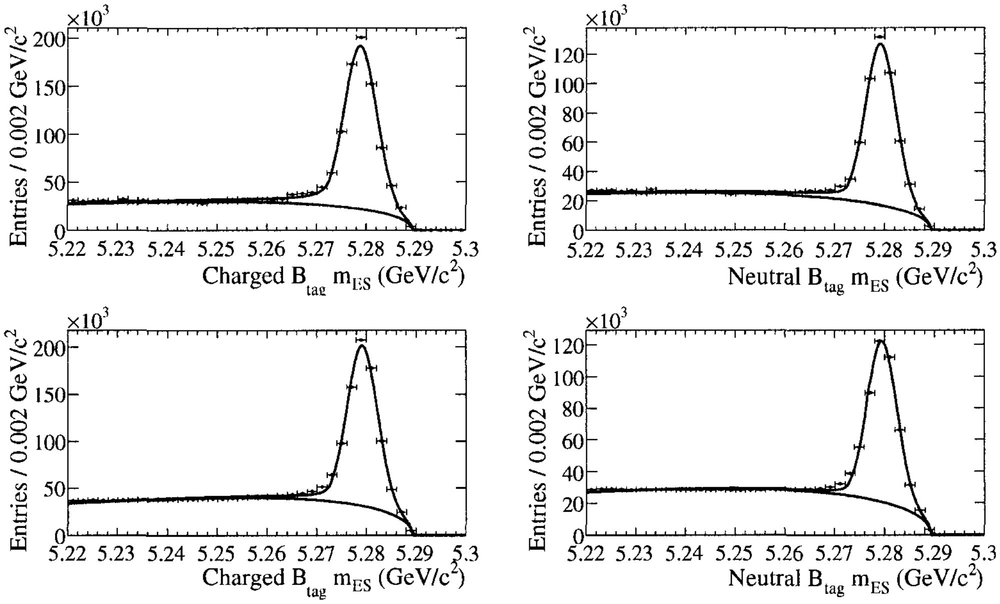

Figure 6–1: m_{ES} distributions are fitted with a combination of ARGUS and Crystal Ball to find the peaking component. The top plots are for data, bottom plots for MC.

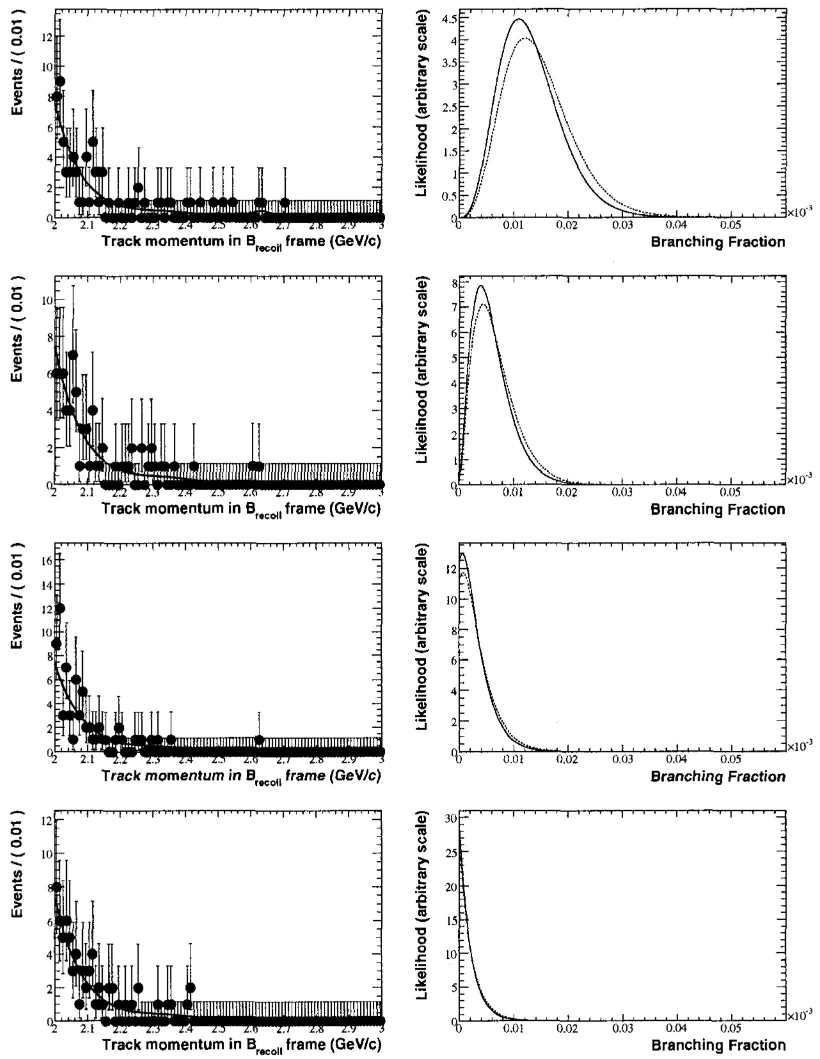

Figure 6–2: The unbinned maximum likelihood fits for varying number of signal events (for five, three, one and zero events, from the top to the bottom) for $B^+ \to e^+\nu_e$ mode.

Gaussian centered at zero and an RMS of unity. No bias corrections are applied to any of the decay modes. A systematic uncertainty rising from the possible bias is set as the average differences between the number of expected events and the quantities given by the fits.

All relevant sources of uncertainties, statistical and systematic, are listed in Table 6–5. The likelihood plots (Figure 6–2) show the likelihood plotted as a function of the branching fraction assumption, with (dotted line) and without (solid line) the systematic uncertainties. This uncertainty is calculated by varying the branching fraction assumption by its total uncertainty, as given by Table 6–5.

Table 6–4: The average numbers (100 trials) of signal and background events for the $B^+ \to e^+\nu$ toy MC. N_{sig} is the total number of signal events in the fit, n_{s} and n_{b} are the the numbers of signal and background events in the signal region.

Generated Signal (N_{gen})	N_{sig} from fit	n_{s} from fit	n_{b} from fit
10	10.07 ± 1.68	8.86 ± 1.48	2.85 ± 0.32
9	9.07 ± 1.19	7.98 ± 1.05	2.86 ± 0.33
8	7.89 ± 1.49	6.94 ± 1.31	2.80 ± 0.32
7	6.81 ± 1.07	5.99 ± 0.94	2.79 ± 0.26
6	5.85 ± 1.24	5.14 ± 0.24	2.75 ± 0.31
5	5.19 ± 1.11	4.57 ± 1.09	2.79 ± 0.21
4	4.02 ± 0.93	3.54 ± 0.98	2.74 ± 0.25
3	2.87 ± 0.93	2.53 ± 0.82	2.73 ± 0.23
2	1.68 ± 1.12	1.48 ± 0.99	2.75 ± 0.26
1	0.80 ± 0.78	0.70 ± 0.69	2.87 ± 0.23
0	-0.13 ± 0.29	-0.11 ± 0.26	2.83 ± 0.15

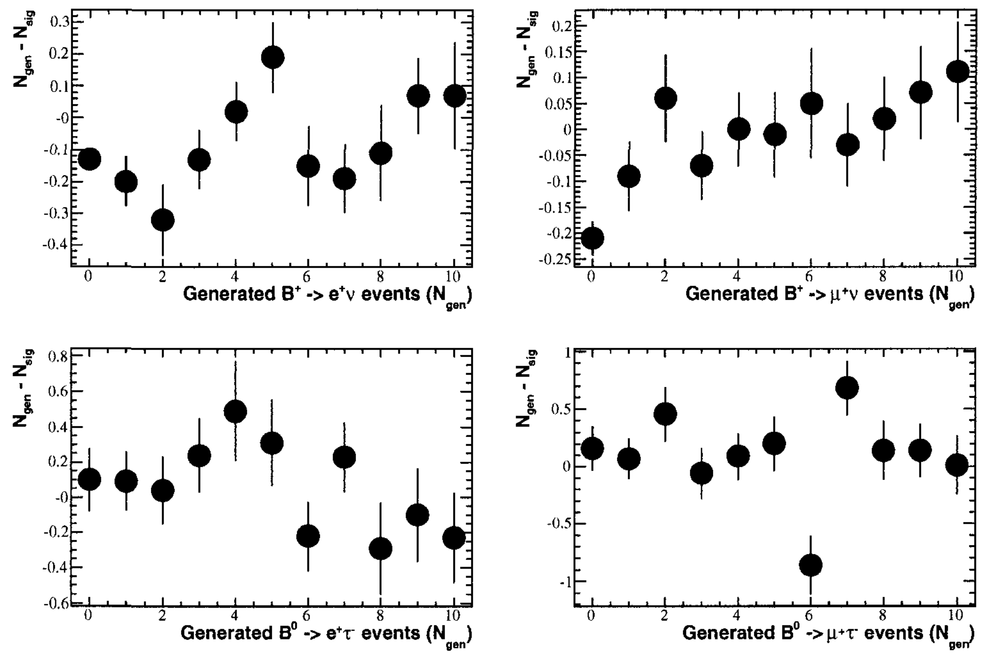

Figure 6–3: The bias, $N_{\text{gen}} - N_{\text{sig}}$, as a function of N_{gen}.

Table 6–5: The sources and magnitudes of systematic uncertainties, in percent (%).

	Signal Mode, $B \to \ldots$			
Uncertainty source	$e^+ \tau^-$	$\mu^+ \tau^-$	$e^+ \nu$	$\mu^+ \nu$
Signal PDF	5.6	10.6	4.3	8.2
Background PDF	3.9	3.1	5.1	7.8
B_{tag} efficiency	6.4	6.4	5.8	5.8
PID efficiency	5.3	5.8	1.0	2.0
MC Statistics	8.6	7.4	3.0	2.8
Tracking efficiency	1.7	1.7	0.8	0.8
$N_{B\bar{B}}$	1.1	1.1	1.1	1.1

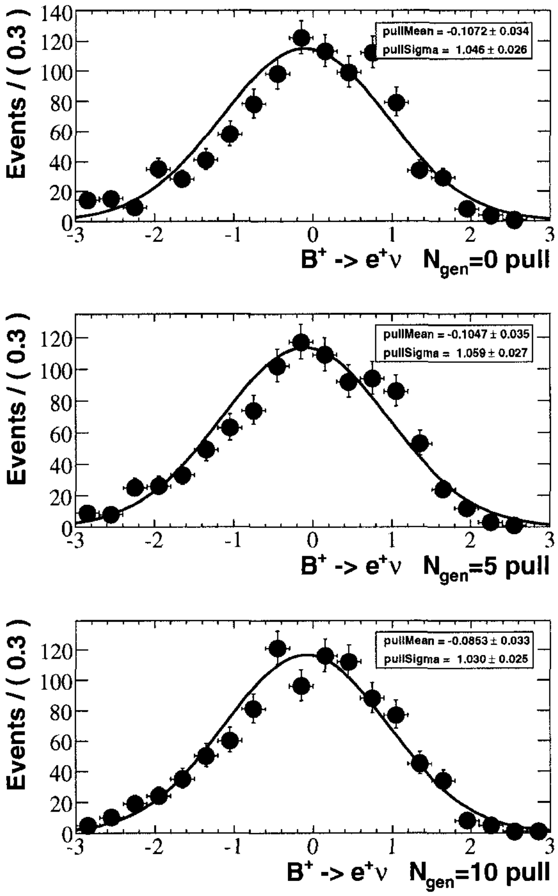

Figure 6–4: Sample distributions for the pull, $(N_{\text{gen}} - N_{\text{sig}})/\sigma_{\text{fit}}$, for $B^+ \to e^+\nu$.

CHAPTER 7
Results

We have presented the searches for the rare leptonic decays $B^+ \to \ell^+\nu$ and $B^0 \to \ell^\pm\tau^\mp$, where $\ell = e, \mu$, using a novel hadronic tag reconstruction technique. While a high luminosity sample preferred for this technique is not yet available, we have shown that the clean signal signature, greatly suppressed background, and a good handle on systematic uncertainties provide promise at studies with higher statistics. We extract the signal using a maximum likelihood fit to the signal lepton candidate momentum in the signal B rest frame (see Figure 7–1), and find no evidence of signal in any of the decay modes in a data sample of approximately 378 million $B\overline{B}$ pairs ($342\,\mathrm{fb}^{-1}$). We set the branching fraction upper limits at $\mathcal{B}(B^+ \to e^+\nu) < 5.2 \times 10^{-6}$, $\mathcal{B}(B^+ \to \mu^+\nu) < 5.6 \times 10^{-6}$, $\mathcal{B}(B^0 \to e^+\tau^-) < 2.8 \times 10^{-5}$ and $\mathcal{B}(B^0 \to \mu^+\tau^-) < 2.2 \times 10^{-5}$, at 90% confidence level. While these upper limits on $\mathcal{B}(B^+ \to e^+\nu)$ and $\mathcal{B}(B^+ \to \mu^+\nu)$ complement the more stringent limits available from inclusive studies [22, 24], the $B^0 \to e^+\tau^-$ and $B^0 \to \mu^+\tau^-$ results are the most stringent upper limits available.

The signal selection efficiencies, the expected number of background events and the fit results on the data are listed in Table 7–1 with their statistical uncertainties. The calculated values for $\mathcal{B}$, including all statistical and systematic effects, are also listed.

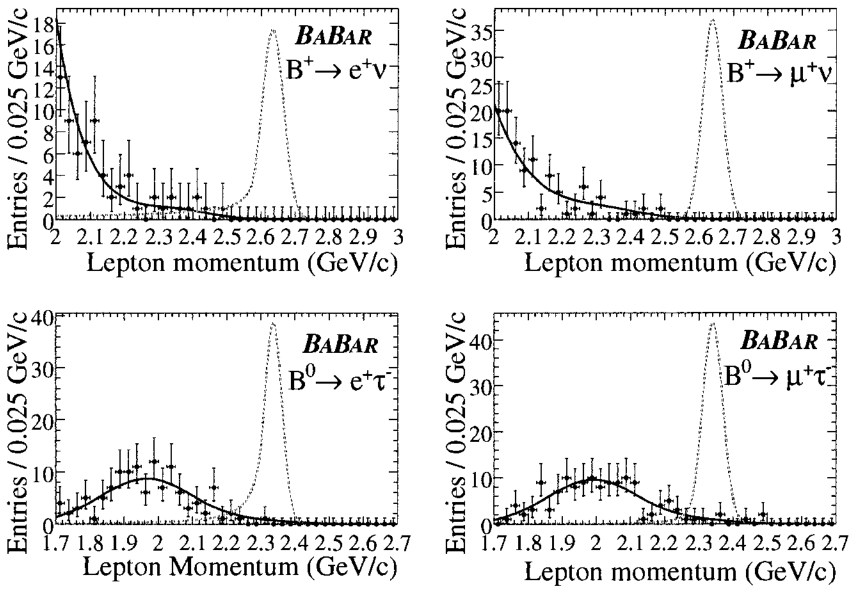

Figure 7–1: The unbinned maximum likelihood fits on the lepton momentum. The green dashed line represents the signal PDF.

Table 7–1: Important physics quantities: the signal selection efficiency, ϵ_{tot}, with its statistical uncertainty, as determined by the signal MC; the number of signal and background events in the signal regions, n_s^* and n_b^*, as given by the fits; the branching fractions are shown with uncertainties including all statistical and systematic effects.

Quantity	Signal Mode, $B \to ...$			
	$e^+\nu$	$\mu^+\nu$	$e^+\tau^-$	$\mu^+\tau^-$
Selection Eff. ($\times 10^5$)	139 ± 4	124 ± 4	32 ± 2	27 ± 2
n_b^* MC	2.66 ± 0.13	5.74 ± 0.25	8.69 ± 0.27	12.14 ± 0.45
n_b^* Fit Data	2.67 ± 0.19	5.67 ± 0.34	9.35 ± 0.35	13.03 ± 0.31
n_s^* Fit Data	-0.07 ± 0.03	-0.11 ± 0.05	0.02 ± 0.01	0.01 ± 0.01
$\mathcal{B} \times 10^{-6}$	$-0.1^{+2.6}_{-1.7}$	$-0.2^{+2.7}_{-1.8}$	0^{+15}_{-10}	0^{+11}_{-7}
$\mathcal{B}^{90\% C.L}$	5.2×10^{-6}	5.6×10^{-6}	2.8×10^{-5}	2.2×10^{-5}

The branching fraction upper limits, for both $B^+ \to \ell^+\nu$ and $B^0 \to \ell^+\tau^-$ modes, can be used to constrain SUSY parameters such as $\tan\beta$ and the Higgs boson masses. Considering the SUSY seesaw model with degenerate right-handed neutrino masses with $M_N = 10^{14}$ GeV, all SUSY-breaking mass parameters being equal at low scales, and assuming $(Y_\nu^\dagger Y_\nu)_{32} = 1$ [9, 40], we get an approximation:

$$\mathcal{B}(B^0 \to \mu^+\tau^-) \sim 1.8 \times 10^{-8} \left(\frac{\tan\beta^8}{60}\right) \left(\frac{100\,\text{GeV}}{M_A}\right)^4, \tag{7.1}$$

where M_A is the mass of the Higgs boson A^0. Using this relation, we plot the $\tan\beta$ as a function of the M_A. As seen in Figure 7–2, assuming $M_A \sim 150$ GeV allows us to set a constraint $\tan\beta < 162$, at 90% C.L.. An improvement on the branching fraction upper limit by two orders of magnitude ($\mathcal{B}(B^0 \to \mu^+\tau^-) < 2.2 \times 10^{-7}$), an improvement well within the potential reach of a "Super B" factory, would imply a constraint of $\tan\beta < 91$, at 90% C.L. (Figure 7–3).

Similarly, considering the effect of new physics through charged Higgs mediation in $B^+ \to \ell^+\nu$ decays (see Equation 2.3), we plot $\tan\beta$ against the mass of the charged Higgs Boson, M_H (Figure 7–4).

For the $B^+ \to \ell^+\nu$ modes, the branching fraction upper limits can also be used to constrain the lepton-flavor-violating SUSY one-loop effective couplings, $\Delta_{\mathrm{R}}^{32,31}$. Assuming $\tan\beta = 60$ and using the Equation 2.4 we plot the quantity Δ_{R}^{32} as a function of the M_H. Figure 7–5 shows that assuming $M_H = 500$ GeV allows us to set a constraint $\Delta_{\mathrm{R}}^{32} < 0.057$, at 90% C.L..

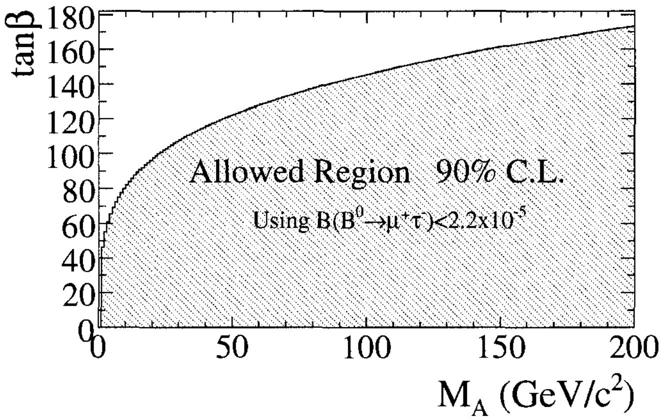

Figure 7–2: The allowed parameter space for $\tan\beta$ and M_A assuming $\mathcal{B}(B^0 \rightarrow \mu^+\tau^-) < 2.2 \times 10^{-5}$.

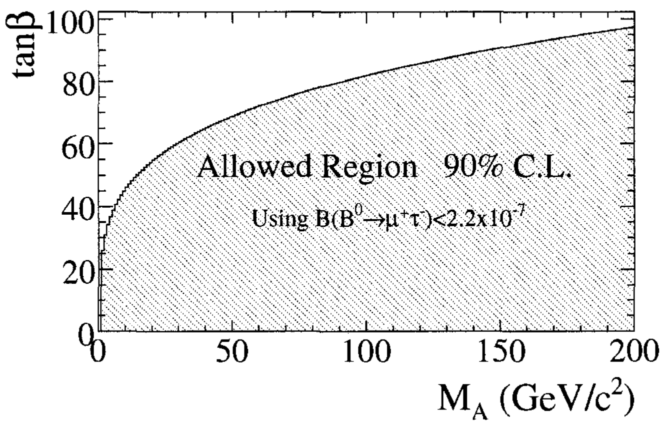

Figure 7–3: The allowed parameter space for $\tan\beta$ and M_A assuming $\mathcal{B}(B^0 \rightarrow \mu^+\tau^-) < 2.2 \times 10^{-7}$.

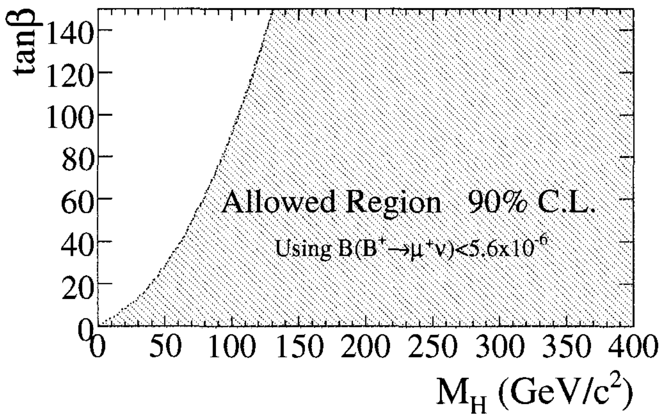

Figure 7–4: The allowed parameter space for $\tan\beta$ and M_H assuming $\mathcal{B}(B^+ \to \mu^+\nu) < 5.6 \times 10^{-6}$.

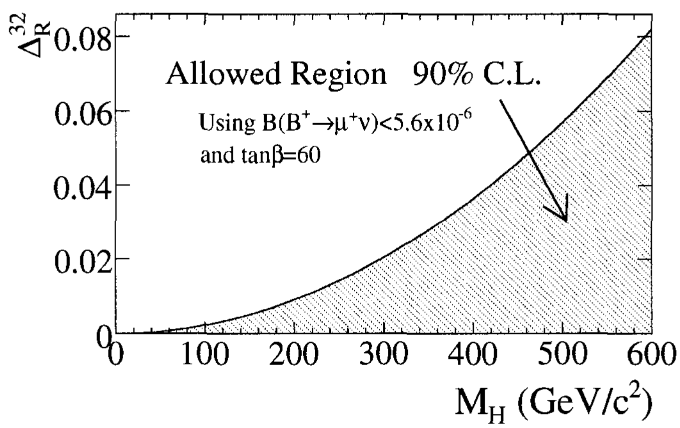

Figure 7–5: The allowed parameter space for Δ_R^{32} and M_H assuming $\mathcal{B}(B^+ \to \mu^+\nu) < 5.6 \times 10^{-6}$ and $\tan\beta = 60$.

CHAPTER 8
APPENDIX

Additional tables and figures.

Table 8–1: The average numbers (100 trials) of signal and background events for the $B^+ \to \mu^+\nu$ toy MC. N_{sig} is the total number of signal events in the fit, n_s and n_b are the numbers if signal and background events in the likelihood calculation region.

Generated Signal (N_{gen})	N_{sig} from fit	n_s from fit	n_b from fit
10	10.11 ± 0.97	9.71 ± 0.93	5.98 ± 0.39
9	9.07 ± 0.89	8.71 ± 0.85	6.05 ± 0.39
8	8.02 ± 0.81	7.67 ± 0.78	5.98 ± 0.42
7	6.97 ± 0.79	6.69 ± 0.76	5.95 ± 0.36
6	6.05 ± 1.06	5.81 ± 1.02	5.92 ± 0.35
5	4.99 ± 0.82	4.79 ± 0.79	5.93 ± 0.30
4	4.00 ± 0.71	3.84 ± 0.68	5.88 ± 0.35
3	2.93 ± 0.66	2.81 ± 0.63	5.83 ± 0.26
2	2.06 ± 0.84	1.98 ± 0.80	5.79 ± 0.30
1	0.91 ± 0.67	0.87 ± 0.64	5.81 ± 0.27
0	-0.11 ± 0.33	-0.11 ± 0.32	6.00 ± 0.29

Table 8–2: The average numbers (100 trials) of signal and background events for the $B^0 \to e^+\tau^-$ toy MC. $N_{\rm sig}$ is the total number of signal events in the fit, $n_{\rm s}$ and $n_{\rm b}$ are the numbers if signal and background events in the likelihood calculation region.

Generated Signal ($N_{\rm gen}$)	$N_{\rm sig}$ from fit	$n_{\rm s}$ from fit	$n_{\rm b}$ from fit
10	9.77 ± 2.56	8.50 ± 2.23	9.24 ± 0.63
9	8.90 ± 2.64	7.74 ± 2.30	9.23 ± 0.59
8	7.71 ± 2.59	6.70 ± 2.25	9.21 ± 0.57
7	7.23 ± 1.99	6.29 ± 1.73	9.13 ± 0.54
6	5.78 ± 1.96	5.02 ± 1.70	9.07 ± 0.53
5	5.31 ± 2.43	4.62 ± 2.11	9.01 ± 0.58
4	4.49 ± 2.81	3.90 ± 2.44	8.98 ± 0.60
3	3.24 ± 2.09	2.82 ± 1.82	8.87 ± 0.50
2	2.04 ± 1.93	1.77 ± 1.68	8.93 ± 0.62
1	1.09 ± 1.66	0.94 ± 1.44	8.98 ± 0.63
0	0.10 ± 1.79	0.09 ± 1.53	8.19 ± 0.75

Table 8–3: The average numbers (100 trials) of signal and background events for the $B^0 \to \mu^+\tau^-$ toy MC. $N_{\rm sig}$ is the total number of signal events in the fit, $n_{\rm s}$ and $n_{\rm b}$ are the numbers if signal and background events in the likelihood calculation region.

Generated Signal ($N_{\rm gen}$)	$N_{\rm sig}$ from fit	$n_{\rm s}$ from fit	$n_{\rm b}$ from fit
10	10.01 ± 2.58	9.41 ± 2.43	12.95 ± 0.58
9	9.14 ± 2.32	8.59 ± 2.18	12.97 ± 0.61
8	8.14 ± 2.61	7.65 ± 2.45	12.88 ± 0.56
7	6.68 ± 2.35	6.28 ± 2.20	12.89 ± 0.51
6	6.14 ± 2.53	5.77 ± 2.38	12.79 ± 0.57
5	5.20 ± 2.31	4.89 ± 2.17	12.72 ± 0.51
4	4.09 ± 2.02	3.84 ± 1.90	12.69 ± 0.50
3	2.94 ± 2.19	2.76 ± 2.06	12.70 ± 0.56
2	2.46 ± 2.38	2.31 ± 2.24	12.66 ± 0.61
1	1.07 ± 1.79	1.01 ± 1.68	12.79 ± 0.74
0	0.16 ± 1.94	0.15 ± 1.82	13.00 ± 0.77

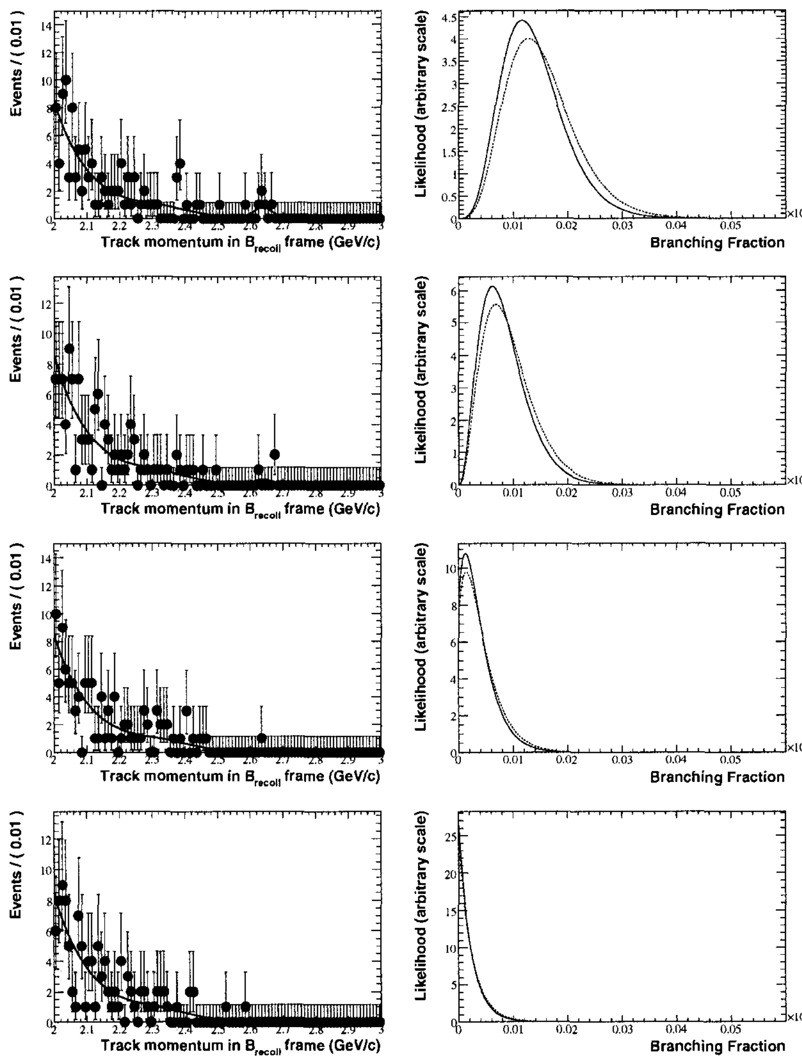

Figure 8–1: The unbinned maximum likelihood fits for varying number of signal events (for five, three, one and zero events, from the top to the bottom) for $B^+ \to \mu^+\nu_\mu$ mode.

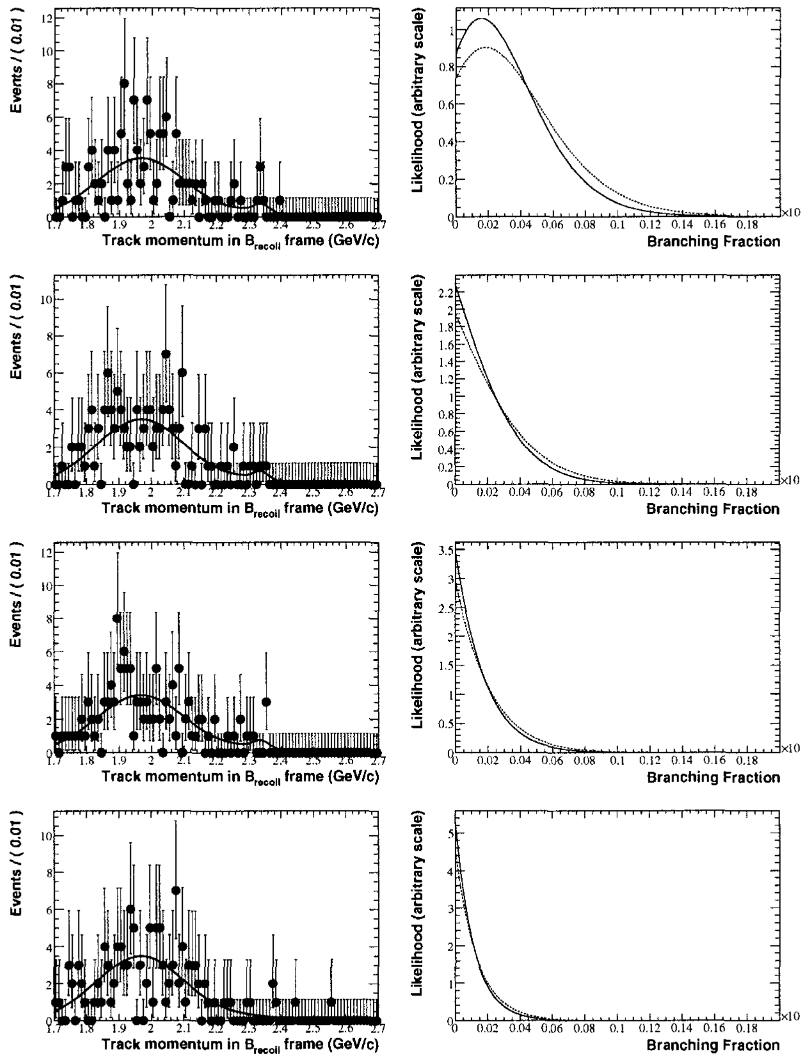

Figure 8–2: The unbinned maximum likelihood fits for varying number of signal events (for five, three, one and zero events, from the top to the bottom) for $B^0 \to e^+\tau^-$ mode.

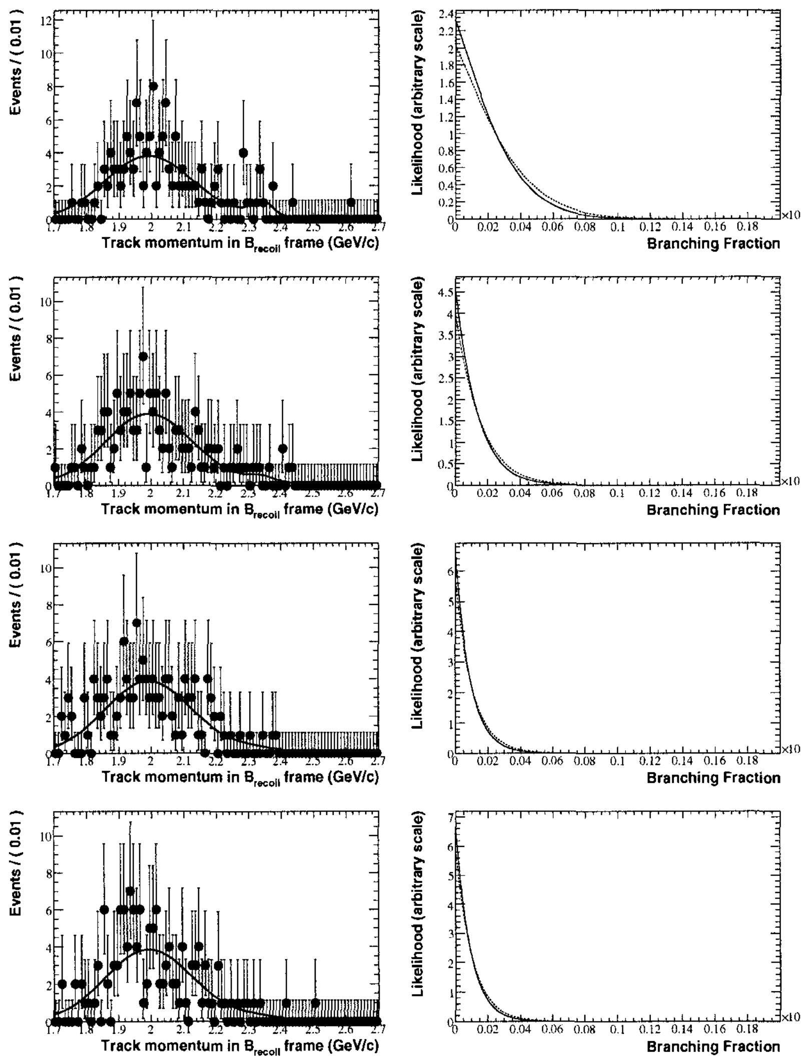

Figure 8–3: The unbinned maximum likelihood fits for varying number of signal events (for five, three, one and zero events, from the top to the bottom) for $B^0 \to \mu^+\tau^-$ mode.

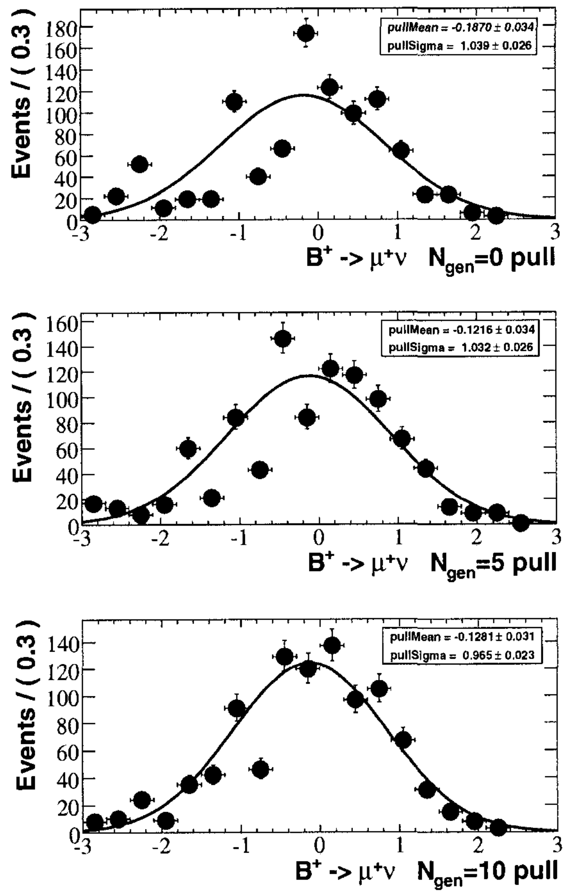

Figure 8–4: Sample distributions for the pull, $(N_{\text{gen}} - N\text{sig})/\sigma_{\text{fit}}$, for $B^+ \to \mu^+\nu$.

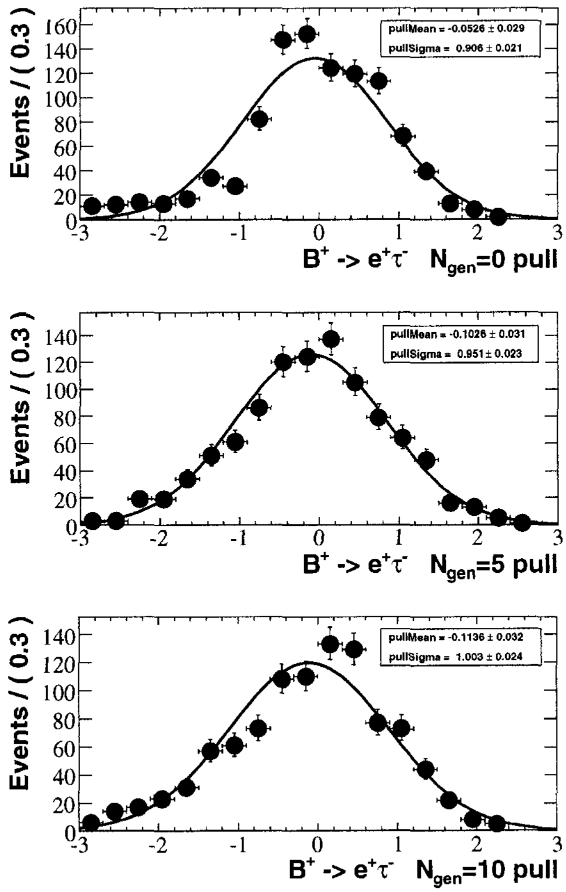

Figure 8–5: Sample distributions for the pull, $(N_{\text{gen}} - N\text{sig})/\sigma_{\text{fit}}$, for $B^0 \to e^+\tau^-$.

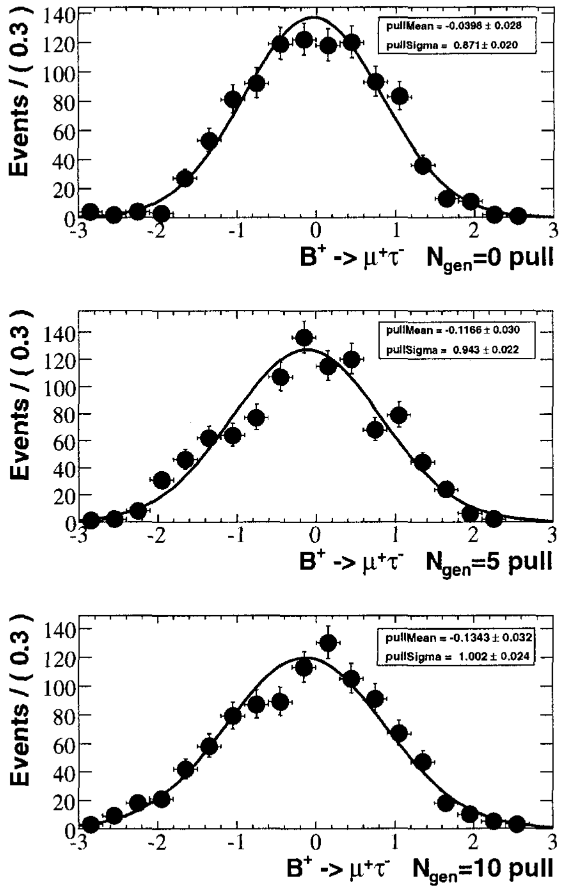

Figure 8–6: Sample distributions for the pull, $(N_{\text{gen}} - N\text{sig})/\sigma_{\text{fit}}$, for $B^0 \to \mu^+\tau^-$.

REFERENCES

[1] Throughout this paper, decay modes imply also their charge conjugates.

[2] Y. Ashie *et al.* (Super-Kamiokande Collaboration), Phys. Rev. **D71**, 112005 (2005); B. Aharmim *et al.* (SNO Collaboration), Phys. Rev. **C72**, 055502 (2005).

[3] Particle Data Group; D. E. Groom *et al.*, Eur. Phys. Jour. C **15**, 1 (2006).

[4] N. Cabibbo, Phys. Lett. **10**, 531 (1963); M. Kobayashi and T. Maskawa, Prog. Theor. Phys. **49**, 652 (1973).

[5] J. Charles *et al.* (CKMfitter group), Eur. Phys. J. **C41**, 1-130 (2005).

[6] S. Albino, F. Deppisch and R. Ruckl, arXiv:hep-ph/0606226v1 (2006); I. Antoniadis, Phys. Lett. B **246**, 377-384 (1990); W.-S. Hou, H. Li, S. Mishima and M. Nagashima, Phys. Rev. Lett. **98**, 131801 (2007).

[7] W.-S. Hou, Phys. Lett. B **296**, 179 (1992); M.Sher and Y.Yuan, Phys. Rev. D **44**, 1461 (1991).

[8] M. Sher, arXiv:hep-ph/9809590 v1 (1998).

[9] A. Dedes, J. Ellis and M. Raidal, arXiv:hep-ph/0209207 v1 (2002).

[10] F. R. Joaquim and A. Rossi, Phys. Rev. Lett. **97**, 181801 (2006).

[11] J. Ellis *et al.*, Phys. Lett. **150B**, 142 (1985).

[12] J.-H. Jang *et al.*, arXiv:hep-ph/9701283 v3 (1996).

[13] A. Masiero and P. Paradisi, arXiv:hep-ph/0609262 v1 (2006).

[14] E. Barberio *et al.* (Heavy Flavor Averaging Group), hep-ex/0603003 (2006).

[15] M. Battaglia *at al.*, arXiv:hep-ph/0304132 v2 (2003).

[16] A. Gray *et al.* (HPQCD Collaboration), Phys. Rev. Lett. **95**, 212001 (2005).

[17] B. Aubert *et al.* (*BABAR* Collaboration), Submitted to PRD hep-ex/0705.1820.

[18] K. Ikado *et al.* (Belle Collaboration), Phys. Rev. Lett. **97**, 251802 (2006).

[19] W.-S. Hou, Phys. Rev. D **48**, 2342 (1993).

[20] A. Masiero and P. Paradisi, arXiv:hep-ph/0609262 v1 (2006).

[21] G. Isidori and P. Paradisi, arXiv:hep-ph/0605012 v2 (2006).

[22] N. Satoyama *et al.* (Belle Collaboration), Phys. Lett. B **647**, 67 (2007).

[23] M. Artuso *et al.* (CLEO Collaboration), Phys. Rev. Lett. **75**, 785 (1995).

[24] B. Aubert *et al.* (*BABAR* Collaboration), Phys. Rev. Lett. **92**, 221803 (2004).

[25] L. J. Hall, R. Rattazzi and U. Sarid, Phys. Rev. D **50**, 7048 (1994).

[26] A. Masiero and P. Paradisi, arXiv:hep-ph/0511289 v2 (2006).

[27] A. Bornheim *et al.* (CLEO Collaboration), arXiv:hep-ex/0408011 v1 (2004).

[28] K. S. Babu and C. Kolda, Phys. Rev. Lett. **89** 241802 (2002); A. Brignole and A. Rossi, Phys Rev. Lett. B **566** 217 (2003).

[29] B. Aubert *et al.* (*BABAR* Collaboration), Nucl. Instrum. Meth. **A479**, 1 (2002).

[30] "The *BABAR* physical book" (*BABAR* Collaboration), Technical Report SLAC-R-504 (1998).

[31] S. Agostinelli *et al.*, Nucl. Instr. Meth. **A506**, 250 (2003).

[32] B. Aubert *et. al.* (*BABAR* Collaboration), arXiv:hep-ex/0607110 (2006).

[33] B. Aubert *et al.* (*BABAR* Collaboration), Phys. Rev. Lett. **95**, 041804 (2005).

[34] B. Aubert *et al.* (*BABAR* Collaboration), Phys. Rev. Lett. **94**, 101801 (2005).

[35] G.C. Fox and S. Wolfram, Phys. Rev. Lett., **41** 1581 (1978).

[36] B. Aubert *et al.* (*BABAR* Collaboration), Phys. Rev. Lett. **92**, 071802 (2004).

[37] J.E. Gaiser *et al.* (Crystal Ball Collaboration), SLAC-R-255 (1982).

[38] H. Albrecht *et al.* (ARGUS Collaboration), Phys. Lett. B **241**, 278 (1990).

[39] "Tracking Efficiency Studies" (*BABAR* Collaboration), *BABAR* Analysis Document #867 v2, (2004).

[40] K. S. Baba and C. Kolda, arXiv:hep-ph/0206310 v2 (2002).